A&A 650, A98 (2021)
https://doi.org/10.1051/0004-6361/202040187

Astronomy & Astrophysics

Prospects for observing the low-density cosmic web in Lyman-α emission

Joris Witstok[1,2,3], Ewald Puchwein[1,2,4], Girish Kulkarni[1,2,5], Renske Smit[2,3,6], and Martin G. Haehnelt[1,2]

[1] Institute of Astronomy, University of Cambridge, Madingley Road, Cambridge CB3 0HA, UK
e-mail: jnw30@cam.ac.uk
[2] Kavli Institute for Cosmology, University of Cambridge, Madingley Road, Cambridge CB3 0HA, UK
[3] Cavendish Laboratory, University of Cambridge, 19 JJ Thomson Avenue, Cambridge CB3 0HE, UK
[4] Leibniz Institute for Astrophysics, An der Sternwarte 16, 14482 Potsdam, Germany
[5] Tata Institute of Fundamental Research, Homi Bhabha Road, Mumbai 400005, India
[6] Astrophysics Research Institute, Liverpool John Moores University, 146 Brownlow Hill, Liverpool L3 5RF, UK

Received 21 December 2020 / Accepted 16 March 2021

ABSTRACT

Mapping the intergalactic medium (IGM) in Lyman-α emission would yield unprecedented tomographic information on the large-scale distribution of baryons and potentially provide new constraints on the UV background and various feedback processes relevant to galaxy formation. In this work, we use a cosmological hydrodynamical simulation to examine the Lyman-α emission of the IGM resulting from collisional excitations and recombinations in the presence of a UV background. We focus on gas in large-scale-structure filaments in which Lyman-α radiative transfer effects are expected to be moderate. At low density the emission is primarily due to fluorescent re-emission of the ionising UV background as a result of recombinations, while collisional excitations dominate at higher densities. We discuss prospects of current and future observational facilities to detect this emission and find that the emission of filaments of the cosmic web are typically dominated by the halos and galaxies embedded in these filaments, rather than by the lower-density filament gas outside halos. Detecting filament gas directly would require a very long exposure with a MUSE-like instrument on the ELT. Our most robust predictions that act as lower limits indicate this would be slightly less challenging at lower redshifts ($z \lesssim 4$). We also find that there is a large amount of variance between fields in our mock observations. High-redshift protoclusters appear to be the most promising environment to observe the filamentary IGM in Lyman-α emission.

Key words. intergalactic medium – large-scale structure of Universe – diffuse radiation – cosmology: theory – methods: numerical

1. Introduction

As the reservoir of the majority of baryons in the Universe, the intergalactic medium (IGM) presents an invaluable means to understanding the evolution of cosmic structure (Meiksin 2009). The IGM has been detected in absorption at a wide range of overdensities out to redshift $z \sim 6$ using H I Lyman-α (Lyα) absorption lines in the spectra of background quasars. Successively larger numbers of quasars have been targeted for this purpose, resulting in a large data set of Lyα absorption measurements of the IGM. Before reionisation is completed, understanding the physical state of the IGM is complicated by the rather uncertain details of the emergence of the first stars, black holes, and galaxies during the epoch of reionisation, but the post-reionisation ($z \lesssim 5.5$) IGM should be well described by cosmological hydrodynamical simulations (Cen et al. 1994; Hernquist et al. 1996; Weinberg et al. 1999; Oñorbe et al. 2017, 2019; Lukić et al. 2015; Bolton et al. 2017). In these simulations, the observed properties of the IGM are reproduced by a fluctuating gas density distribution tracing the cosmic structure formation process. The gas is thereby in ionisation equilibrium with a uniform UV background (UVB) created by galaxies and active galactic nuclei (AGN). This has led to constraints on the ionisation and thermal state of the IGM out to $z \sim 6$ (Rauch et al. 1997; Davé et al. 1999; Schaye et al. 2000; Meiksin & White 2003; Faucher-Giguère et al. 2008; Becker et al. 2011; Bolton et al. 2012; Becker & Bolton 2013; Garzilli et al. 2017; Walther et al. 2019; Khaire et al. 2019) derived from Lyα absorption observations.

In contrast, Lyα emission from the IGM has received relatively little attention, despite a history of just over half a century of theoretically predicted prospects (Partridge & Peebles 1967; Hogan & Weymann 1987; Gould & Weinberg 1996; Fardal et al. 2001; Furlanetto et al. 2003, 2005; Cantalupo et al. 2005; Kollmeier et al. 2010; Faucher-Giguère et al. 2010; Rosdahl & Blaizot 2012; Silva et al. 2013, 2016; Heneka et al. 2017; Augustin et al. 2019; Elias et al. 2020). Observing intergalactic Lyα emission instead of absorption has distinct advantages. First, unlike absorption Lyα emission is directly sensitive to the recombination and collisional physics of the neutral as well as the ionised hydrogen content of the IGM and the circumgalactic medium (CGM) that feeds the formation and evolution of galaxies. Second, observations of the Lyα emission allow us to homogeneously probe three-dimensional volumes. Although three-dimensional Lyα-forest studies have now become possible owing to the high number density of observed bright quasars (see e.g., Cisewski et al. 2014), the number of such quasars drops rapidly towards high redshifts (Kulkarni et al. 2019b). Third, observations of Lyα emission can potentially provide independent constraints on the IGM temperature and photoionisation rate, particularly at densities higher than those probed by the Lyα forest ($\Delta \gtrsim 10$).

Using narrowband imaging and integral field unit (IFU) imaging, emission in Lyα from the CGM and/or IGM has now been observed as 'giant Lyα nebulae' in the proximity (~100 kpc) of radio-loud and radio-quiet quasars (Djorgovski et al. 1985; Hu et al. 1991; Heckman et al. 1991; McCarthy et al. 1990; Venemans et al. 2007; Villar-Martín et al. 2007; Cantalupo et al. 2008, 2012, 2014; Humphrey et al. 2008; Rauch et al. 2008, 2011, 2013; Sánchez & Humphrey 2009; Martin et al. 2014; Roche et al. 2014; Hennawi et al. 2015; Arrigoni Battaia et al. 2016; Borisova et al. 2016; Fumagalli et al. 2016; Cantalupo 2017). The circumgalactic hydrogen is strongly affected by ionising radiation from these quasars. Observations suggest that the Lyα emission is mostly recombination radiation and that dense ($n > 1\,\mathrm{cm}^{-3}$), ionised, and relatively cold ($T \sim 10^4$ K) pockets of gas should surround massive galaxies (Cantalupo 2017).

Lyα emission can also result from fluorescent re-emission of the ionising UVB radiation. In the last two decades, significant progress has been made in detecting extended Lyα emission around galaxies (Francis et al. 1996; Fynbo et al. 1999; Keel et al. 1999; Steidel et al. 2000, 2011; Hayashino et al. 2004; Rauch et al. 2008; Matsuda et al. 2012; Prescott et al. 2013; Momose et al. 2014; Geach et al. 2016; Wisotzki et al. 2016, 2018; Cai et al. 2017; Leclercq et al. 2017; Vanzella et al. 2017; Oteo et al. 2018; Arrigoni Battaia et al. 2019). Using deep (~30 h exposure time) VLT/MUSE observations of the *Hubble* Deep Field South (HDFS) and *Hubble* Ultra-Deep Field (HUDF) reported in Bacon et al. (2015, 2017), the sensitivity of median-stacked radial profiles of Lyα emission currently reaches a surface brightness (SB) of $\sim 4 \cdot 10^{-21}\,\mathrm{erg\,s^{-1}\,cm^{-2}\,arcsec^{-2}}$ (Wisotzki et al. 2018). This faint signal from Lyα halos can be traced out to projected (physical) galactic radii of ~60 kpc (Wisotzki et al. 2018). Even deeper data sets, such as the MUSE Ultra Deep Field (MUDF, described in Lusso et al. 2019) and the MUSE Extremely Deep Field (MXDF, see Bacon et al. 2021) are beginning to be explored. Both will reach a depth of the order of ~100 h (i.e. reaching a sensitivity of the order of a few times $10^{-20}\,\mathrm{erg\,s^{-1}\,cm^{-2}\,arcsec^{-2}}$). The Ly$\alpha$ emission coming from the intergalactic gas between galaxies is just beginning to be probed and is the focus of this work.

So far, it has proven very difficult to map the spatial distribution of the IGM beyond the CGM and to study its global properties by directly observing the IGM in emission rather than absorption. This has so far only been achieved in special cases, for example in the vicinity of AGN (e.g., Cantalupo et al. 2014; Martin et al. 2014; Hennawi et al. 2015; Borisova et al. 2016; Umehata et al. 2019), by applying statistical image processing techniques (Gallego et al. 2018, in this case, the CGM only showed a preferential direction of extension towards neighbouring galaxies, no significant signal of filamentary structure in the IGM was found), by cross-correlating Lyα emitters (LAEs) and Lyα intensity mapping (Kakuma et al. 2019), by observing the thermal Sunyaev-Zel'dovich effect (e.g., de Graaff et al. 2019; Tanimura et al. 2019), or by detection of warm-hot gas in X-ray emission (e.g., Kull & Böhringer 1999; Eckert et al. 2015).

Building on the work of previous studies (such as those by Gould & Weinberg 1996; Furlanetto et al. 2003; Cantalupo et al. 2005; Silva et al. 2013, 2016), this work investigates the possibility of such observations. We explore a simulation run based on the Sherwood simulation project (Bolton et al. 2017), which incorporates an on-the-fly self-shielding model to predict the properties of Lyα emission from the cosmic web. The simulation is aimed at accurately modelling the IGM and employs a modified version of the uniform metagalactic UVB model by Haardt & Madau (2012; HM12 hereafter) that is calibrated to match observations of the Lyα forest. The large volume and high dynamic range of the simulation allows us to probe the physical environment of the IGM with well-resolved under- and overdense regions. Moreover, this enables us to study the prospects of an array of current and future observational facilities aiming to detect this emission. We focus on a future reincarnation of VLT/MUSE on next-generation observatories such as the Extremely Large Telescope (ELT) for a more detailed sensitivity analysis.

We describe the simulations used in this work in Sect. 2, together with our model for Lyα production in the IGM. Sect. 3 presents our results and a discussion of the detection prospects. We summarise our conclusions in Sect. 4. Throughout this work, we adopt the cosmological parameters $\Omega_\mathrm{m} = 0.308$, $\Omega_\Lambda = 0.692$, $\Omega_\mathrm{b} = 0.0482$, and $h = 0.678$ (so $H_0 = 67.8\,\mathrm{km\,s^{-1}\,Mpc^{-1}}$), taken from the best-fitting ΛCDM model for the combined *Planck*+WP+highL+BAO measurements (Planck Collaboration XVI 2014). The helium fraction is assumed to be $f_\mathrm{He} = 0.24$.

2. Methodology

Lyα emission from the moderately dense IGM is produced via recombinations and collisional excitations. Recombination is the process in which a free electron is captured by an ion, which in this case is H II. Lyα is emitted provided the recombination leaves hydrogen in an excited state and the last step of the resulting series of energy transition(s) is from energy level $n = 2$ to $n = 1$. Collisional excitation is the effect in which neutral hydrogen (H I) is excited through a collision with an electron, which can subsequently lead to the emission of Lyα in the same way as with recombinations. We used a hydrodynamical simulation calibrated to UVB constraints from the Lyα forest along with an on-the-fly self-shielding prescription to model these processes.

In the analysis, we focus on low-density gas (below the critical density above which self-shielding becomes a dominant process) as we are primarily interested in detecting emission from the cosmic web. At $z = 4.8$, this critical density corresponds to an overdensity $\Delta \equiv \rho/\bar{\rho} \simeq 100$ (see Sect. 2.2.2). Furthermore, modelling of all relevant feedback and radiative transfer effects becomes increasingly challenging at higher densities.

2.1. Lyα emission through recombination

2.1.1. Emissivity

The underlying equation governing Lyα emission resulting from recombination in a gas containing hydrogen is given by (see e.g., Dijkstra 2014; Silva et al. 2016)

$$\epsilon_\mathrm{rec}(T) = f_\mathrm{rec,A/B}(T)\, n_\mathrm{e}\, n_\mathrm{HII}\, \alpha_\mathrm{A/B}(T)\, E_\mathrm{Ly\alpha}, \quad (1)$$

where ϵ_rec is the Lyα luminosity density (in units of $\mathrm{erg\,s^{-1}\,cm^{-3}}$) as a function of the temperature T of the gas. In this equation, $f_\mathrm{rec,A/B}$ is the fraction of case-A or case-B recombinations, which ultimately result in the emission of a Lyα photon; and the free electron and H II number densities are denoted by n_e and n_HII, respectively. Case A and case B refer to the way in which recombination occurs. All possible recombinations of H II and a free electron are considered in case A; this includes any recombination event that take the resulting neutral hydrogen directly to the ground state ($n = 1$). In case B, only recombinations resulting in hydrogen in an excited state are considered. The recombination coefficient given in unit volume per unit time ($\mathrm{cm^3\,s^{-1}}$) for

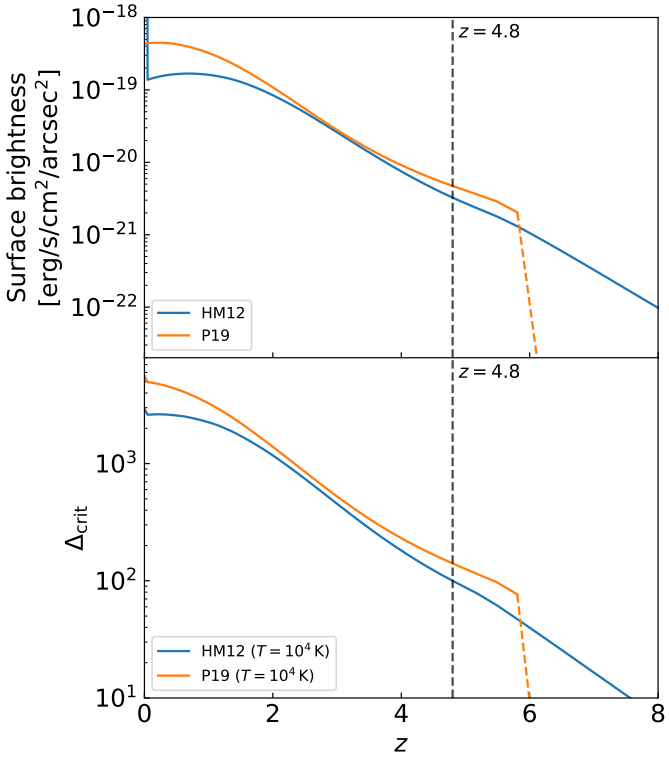

Fig. 1. Limiting SB and density quantities as a function of redshift. The *top panel* shows the limiting SB of Lyα in the mirror assumption, where 65% of ionising photons in the UVB are reprocessed into Lyα photons (see text for details) and the *bottom panel* shows the self-shielding critical density contrast $\Delta_{\rm crit}$. The two different lines correspond to UVBs of Haardt & Madau (2012, HM12) and Puchwein et al. (2019, P19). Above $z > 6$, where the line is dashed, the P19 limits are not representative of ionised bubbles during patchy reionisation because the impact of neutral regions on the effective opacity to hydrogen ionising photons is included in the modelling (see P19) and hence a neutral hydrogen-weighted average over both neutral and ionised regions is computed in that model. A redshift of $z = 4.8$ is highlighted by the dashed line.

case-A or -B recombination is denoted by $\alpha_{\rm A/B}$, and $E_{\rm Ly\alpha}$ is the energy of a Lyα photon.

Since direct recombinations into the ground state do not result in Lyα emission, an appropriately lower fraction that results in Lyα emission, $f_{\rm rec,A} < f_{\rm rec,B}$, has to be used if $\alpha_{\rm A}$ rather than $\alpha_{\rm B}$ is adopted as the recombination coefficient. The luminosity densities obtained for case A and case B are then equivalent, except for minor differences due to different fitting functions for the coefficients. We chose to fix our calculations to use case-B coefficients. We modelled $f_{\rm rec,B}$ using the relations given by Cantalupo et al. (2008) and Dijkstra (2014), whose fitting formulae are presented in Appendix A; for example at $T = 10\,000$ K, this fraction is ~0.68. We elected to use case B because the model for $f_{\rm rec,A}(T)$ from Dijkstra (2014) is only valid up to $\sim 10^{6.5}$ K, whereas gas temperatures in our simulations range up to $\sim 10^7$ K (Sect. 3.2). For the recombination coefficient, $\alpha_{\rm B}(T)$, we adopted the fitting function given in Draine (2011). The precise expressions can also be found in Appendix A.

2.1.2. Mirror limit

In the absence of local ionising UV sources and significant collisional ionisation, the recombination contribution to Lyα emission should not exceed the SB expected from fully absorbing the external UVB at the boundaries of self-shielded regions and fluorescently re-emitting a corresponding number of Lyα photons, hence 'mirroring' the external UVB. In calculating the recombination contribution to Lyα emission, unless mentioned otherwise, we employed this mirror assumption as an upper limit. More precisely, we placed an upper SB limit at the value expected when 65% of the ionising UVB is reprocessed as Lyα photons (e.g., Gould & Weinberg 1996; Cantalupo et al. 2005), equal to SB $\simeq 3.29 \cdot 10^{-21}$ erg s^{-1} cm^{-2} arcsec^{-2} for a HM12 UVB at $z = 4.8$. Fig. 1 shows the mirror limit for two different UVBs from HM12 and Puchwein et al. (2019; P19 hereafter).

In reality, local ionising sources can boost the recombination emission above the mirror limit. Predicting this reliably is, however, extremely challenging because it involves modelling the ionising source populations in galaxies and the escape of ionising radiation from galaxies in full detail. Our recombination contribution to Lyα emission computed assuming the mirror limit should hence be considered only as a robust lower limit.

2.2. Lyα emission through collisional excitation

2.2.1. Emissivity

For collisional excitation, the Lyα luminosity density has a similar form (Scholz et al. 1990; Scholz & Walters 1991; Dijkstra 2014; Silva et al. 2016) given by

$$\epsilon_{\rm exc}(T) = \gamma_{\rm 1s2p}(T)\, n_{\rm e}\, n_{\rm HI}\, E_{\rm Ly\alpha}, \tag{2}$$

where $n_{\rm HI}$ denotes the number density of neutral hydrogen. We used the fitting functions for the collisional excitation coefficient $\gamma_{\rm 1s2p}$ given by Scholz et al. (1990) and Scholz & Walters (1991). These fitting functions are valid in the temperature range $2 \cdot 10^3\,{\rm K} \leq T \leq 1 \cdot 10^8\,{\rm K}$ (cf. Appendix A). The rates are not identical to those applied in the cosmological hydrodynamical simulation (see Sect. 2.4) as these are only given as an ensemble rather than for the specific $2p \rightarrow 1s$ transition in which Lyα is emitted, but in the relevant temperature regime deviate so little that gas cooling equilibrium would not be appreciably violated.

2.2.2. Density limits

When computing the Lyα luminosity due to collisional excitation, we only considered gas well below the critical self-shielding density that is derived for the appropriate UVB (the HM12 UVB, unless mentioned otherwise). We made use of the critical self-shielding hydrogen number density at $T = 10^4$ K given in Eq. (13) in Rahmati et al. (2013) for this purpose (shown in the bottom panel of Fig. 1 as a density contrast), but since this is based on the column density distribution of neutral hydrogen and for the purpose of absorption instead of emission processes, we chose a conservative default density threshold at half this value.

As shown in Fig. 1, the critical self-shielding overdensity is $\Delta_{\rm crit} \simeq 100$ at $z = 4.8$. We note that the density contrast, $\Delta_{\rm crit}$, decreases towards higher redshift, meaning gas starts to be affected by self-shielding at a lower overdensity at higher redshift. By focussing on gas with densities below this critical threshold, we additionally ensure at this redshift that we do not enter the realm of gas densities strongly affected by the detailed baryonic physics of galaxy formation, such as feedback processes. For this reason, most of the results presented in this work are chosen to be at $z = 4.8$ and are again a robust lower limit.

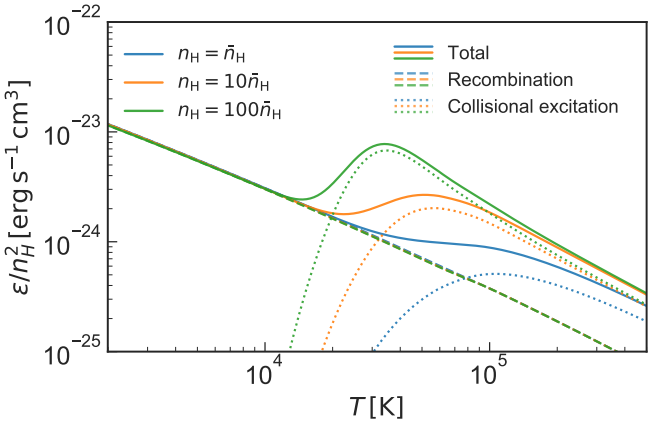

Fig. 2. Normalised emissivity (units are erg s^{-1} cm^3) of the Lyα line in a cloud of primordial gas at $z = 4.8$ as a result of recombination and collisional excitation processes as a function of temperature. There are three values of density, corresponding to overdensities of 1, 10, and 100, respectively; the mean cosmological hydrogen density corresponds to $\bar{n}_H = 3.69 \cdot 10^{-5}$ cm^{-3} at this redshift. The dashed and dotted lines show the contribution from just recombination and collisional excitation, respectively.

2.3. Emissivity

Figure 2 shows the Lyα luminosity density at $z = 4.8$ as a function of gas temperature for a gas of primordial composition at three different overdensities of 1, 10, and 100; the mean cosmological hydrogen density corresponds to $\bar{n}_H = 3.69 \cdot 10^{-5}$ cm^{-3} at this redshift. To derive the corresponding neutral hydrogen densities, we assume that hydrogen is in ionisation equilibrium with the HM12 UVB at $z = 4.8$. Figure 2 also shows the recombination and collisional excitation components of the total Lyα emission. We find that collisional excitation dominates at high temperatures ($T \gtrsim 2 \times 10^4$ K).

2.4. Cosmological hydrodynamical simulation

To estimate the cosmological Lyα signal with the theoretical framework above, we made use of a simulation that builds upon the Sherwood simulation project (Bolton et al. 2017). The simulation is performed with the energy- and entropy-conserving TreePM smoothed particle hydrodynamics (SPH) code P-GADGET-3, which is an updated version of the publicly available GADGET-2 code (Springel et al. 2001; Springel 2005). In this work, we used the same volume as in the 40–1024 simulation of the Sherwood suite. A periodic, cubic volume $40\,h^{-1}$ cMpc long was simulated, employing a softening length of $l_{\rm soft} = 1.56\,h^{-1}$ ckpc, and 1024^3 dark matter and gas particles. Initial conditions were set up at redshift $z = 99$ and the simulation was evolved down to $z = 2$. In order to speed up the simulation, star formation was simplified using the implementation of Viel et al. (2004) in P-GADGET-3; this method converts gas particles, with temperatures less than 10^5 K and densities of more than a thousand times the mean baryon density, to collisionless stars. This approximation is appropriate for this work as we do not consider the Lyα emission from the interstellar medium of galaxies, where a complex set of Lyα radiative transfer processes need to be accounted for. The ionisation and thermal state of the gas in the simulation is derived by solving for the ionisation fractions under the assumption of an equilibrium with the metagalactic UVB modelled according to HM12. A small modification to this UVB is applied at $z < 3.4$ (see Bolton et al. 2017) to result in IGM temperatures that agree with measurements by Becker et al. (2011). We also accounted for self-shielding of dense gas with an on-the-fly self-shielding prescription based on Rahmati et al. (2013). For each SPH particle and each time step, our modified P-GADGET-3 version computes a suppression factor for the UVB due to self-shielding that is based on the local gas density and uses the parameters given in the first line of Table A1 of Rahmati et al. (2013). This factor is applied to photoionisation and heating rates before they are used in the chemistry and cooling solver. The solver follows photoionisation, collisional ionisation, recombination, and photoheating for gas of a primordial composition of hydrogen and helium, as well as further radiative cooling processes such as collisional excitation, Bremsstrahlung (see Katz et al. 1996 for the relevant equations), and inverse Compton cooling off the cosmic microwave background (Ikeuchi & Ostriker 1986). Metal enrichment and its effect on cooling rates are ignored. We identify dark matter halos in the output snapshots using a friends-of-friends algorithm.

2.4.1. Narrowband images

When calculating the SB, we constructed mock narrowband images of the simulations, which are images that replicate the result of the process of capturing a narrowband image with a telescope, by taking a thin slice of the simulation in a direction parallel to a face of the simulation box and converting the emissivity in the simulation to arrive at a SB map; this is discussed in more detail below. The slice thickness corresponds to an observed wavelength width $\Delta\lambda_{\rm obs}$ of the narrowband. Its redshift range is given by

$$\Delta z = \frac{\Delta\lambda_{\rm obs}}{\lambda_{\rm Ly\alpha}}, \tag{3}$$

which corresponds to a comoving distance

$$\Delta d = \frac{c}{H_0}\int_z^{z+\Delta z} \frac{1}{\sqrt{\Omega_{\rm m}\,(1+z')^3 + \Omega_\Lambda}}\,{\rm d}z'. \tag{4}$$

As a reference value for the observed narrowband width, we used $\Delta\lambda_{\rm obs} = 8.75$ Å, the median value of narrowband widths in the study by Wisotzki et al. (2016); this corresponds to 7 spectral pixels of the VLT/MUSE instrument (Sect. 3.3 describes narrowband imaging in more detail). At a redshift of $z = 4.8$, this results in a comoving line-of-sight distance of $\sim 2.7\,h^{-1}$ cMpc (see Sect. 2.2.2 for an elaboration on the choice of this particular redshift), corresponding to only a small fraction of the total size of the simulation volume. We discuss the effect of varying the narrowband width on the detectability of Lyα further in Sect. 3.4.1.

Using the temperature, density, and ionisation fraction, an emissivity for each individual simulation particle within the narrowband slice can be computed. These emissivities were then converted to luminosities and projected onto a two-dimensional plane using the SPH kernel of the simulation particles, turning them into a luminosity per unit area, which in turn is converted to a SB.

2.4.2. Radiative transfer effects

In the predictions made in this work, Lyα propagation is always treated in the optically thin limit. For the constructed mock narrowband images, it is assumed that Lyα photons are emitted in

an isotropic manner and reach the observer without any scattering. The exact effects that scattering would have are difficult to accurately predict given for example that the effects of dust are poorly constrained. But it is expected that for the filamentary IGM, the difference between our simulations and a model with a physically accurate treatment of radiative transfer is mostly influenced by two competing effects. First, there might be a broadening of the filamentary structure due to scattering in the nearby IGM, causing the signal to become fainter. Second, however, filaments may also be illuminated by Lyα radiation coming from nearby dense structures (where additional radiation is likely to be produced in galaxies) that is scattered in the filament, which would cause the filaments to appear brighter. Simulations including radiative transfer show a mixture of these two effects, where the SB of filaments generally is not affected much or is even boosted private communication, Weinberger, 2019. As the effects of radiative transfer on this work are expected to be moderate, they are assumed not to affect our main findings in a major way; a more detailed discussion on the optical depth of Lyα is included in Appendix B. Future work can detail the precise effects of radiative transfer.

We limit the maximum SB from recombinations to what is expected from purely reprocessing or mirroring the UVB at the boundaries of self-shielded regions (see Sect. 2.1.2). This also mitigates the effect where the absence of radiative transfer can bias the SB upwards in cases in which a sightline crosses several dense structures. In reality, however, with the presence of local ionising sources in such dense regions, an amplification with respect to the reprocessed UVB would likely be present as well. This is also suggested by a comparison of our simulation with a post-processing radiative transfer simulation of the same volume using a local source population similar to that described in Kulkarni et al. (2019a). Still, even with an accurate treatment of radiative transfer, the precise effects in the densest regions may rely considerably on the exact baryonic feedback mechanisms that are operating in these regions.

3. Results

3.1. Luminosity density

Figure 3 shows the redshift evolution of the comoving Lyα luminosity density in our simulation down to $z = 2$. The total luminosity of gas within the entire simulation at densities below half the critical self-shielding density, corresponding to an overdensity $\rho/\bar{\rho} \lesssim 50$ at $z = 4.8$ (see Sect. 2.2.2), roughly corresponding to the IGM, is computed. This is also done separately for the recombination and collisional excitation contributions. We then divide by the (comoving) simulation volume to convert the luminosity to a comoving luminosity density.

Observational measurements at low redshift ($z < 3$), as compiled by Chiang et al. (2019), are included as reference. We note that these data points should not be directly compared to our predictions as we consider only emission from the low-density gas in the IGM. The data consist of estimates of the luminosity density of Lyα emission from galaxies and AGN inferred by Wold et al. (2017) based on a flux-limited sample of LAEs from GALEX data and scaling the Hα galaxy luminosity function measurements (Sobral et al. 2013) out to $z = 2$. Chiang et al. (2019) obtain a measurement on the total Lyα luminosity density from galaxies and AGN as well as an upper limit on the diffuse IGM contribution by cross-correlating the GALEX UV intensity maps with spectroscopic objects in SDSS. A comparison of the measurements from Chiang et al. (2019) and Wold et al. (2017)

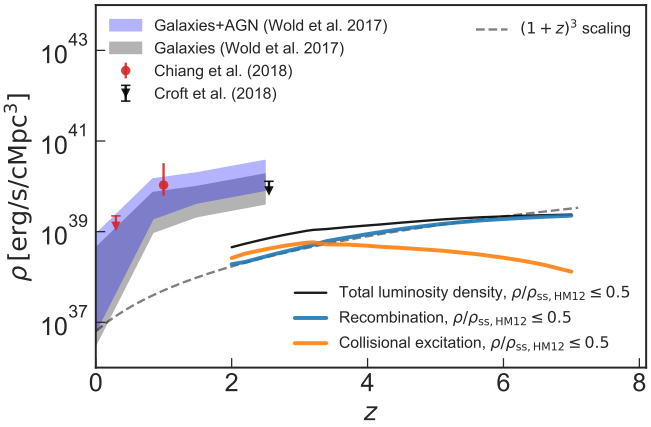

Fig. 3. Redshift evolution of the comoving Lyα luminosity density. The blue and orange lines show the results for recombination and collisional excitation emission for gas at densities below half the critical self-shielding density roughly corresponding to the IGM at an overdensity $\Delta \equiv \rho/\bar{\rho} \lesssim 50$ at $z = 4.8$ (see Sect. 2.2.2). The black line shows the total luminosity density for gas below this density threshold; all these follow from the simulation run with a box size of $40\,h^{-1}$ cMpc and resolution of 2×1024^3 particles (see Sect. 2.4 for more details on the simulation). Observational measurements at low redshift ($z < 3$), as presented in Chiang et al. (2019), have been included as a reference. These consist of luminosity densities of just galaxies and the contribution of galaxies and AGN (shown as the grey and blue shaded areas, respectively) inferred by Chiang et al. (2019) from the intrinsic luminosity density presented in Wold et al. (2017); the measurement and upper limit from Chiang et al. (2019) are shown in red, and the upper limit from Croft et al. (2018) (converted to a luminosity density by Chiang et al. 2019) is shown in black (see text for details). Data points are shown as circles, upper limits as downward triangles. Also shown is the $(1+z)^3$ scaling relation for recombination emission discussed in the text.

indicates that, at least at $z \lesssim 1$, most Lyα emission originates in galaxies and AGN. The upper limit from Croft et al. (2018; converted to a luminosity density by Chiang et al. 2019) is shown in black in Fig. 3. Croft et al. (2018) fit model spectra to luminous red galaxies in BOSS and cross-correlate the residual Lyα emission with the Lyα forest in BOSS quasars to obtain the upper limit from a non-detection shown in Fig. 3. As such, this procedure places a limit on the component of diffuse Lyα emission that correlates with the matter distribution (Croft et al. 2018)[1].

Going from redshift $z = 2$ to $z = 7$, the comoving Lyα luminosity density increases by just under an order of magnitude (see Appendix C for a further discussion of the redshift evolution of SB). As can be seen in the figure, this is mostly due to the increase in recombination emission. Under the simple assumption that the emissivity is produced at a fixed overdensity its emissivity increases like the square of the mean density, which would correspond to a scaling of

$$\epsilon_{\mathrm{rec}} \sim \Delta^2(1+z)^6(\text{physical luminosity density}) \text{ or} \quad (5)$$
$$\epsilon_{\mathrm{rec}} \sim \Delta^2(1+z)^3(\text{comoving luminosity density}),$$

where ϵ_{rec} is the recombination emissivity and $\Delta \equiv \rho/\bar{\rho}$ the overdensity. As shown by the dashed line in Fig. 3, the simple scaling for recombination emission in Eq. (5) explains the simulated luminosity density very well at all redshifts shown.

[1] An additional measurement, arising from a cross-correlation with BOSS quasars, is restricted to scales within $15\,h^{-1}$ cMpc of a quasar (equivalent to only ~3% of space, see Croft et al. 2018) and is therefore not included as a global luminosity density in this work.

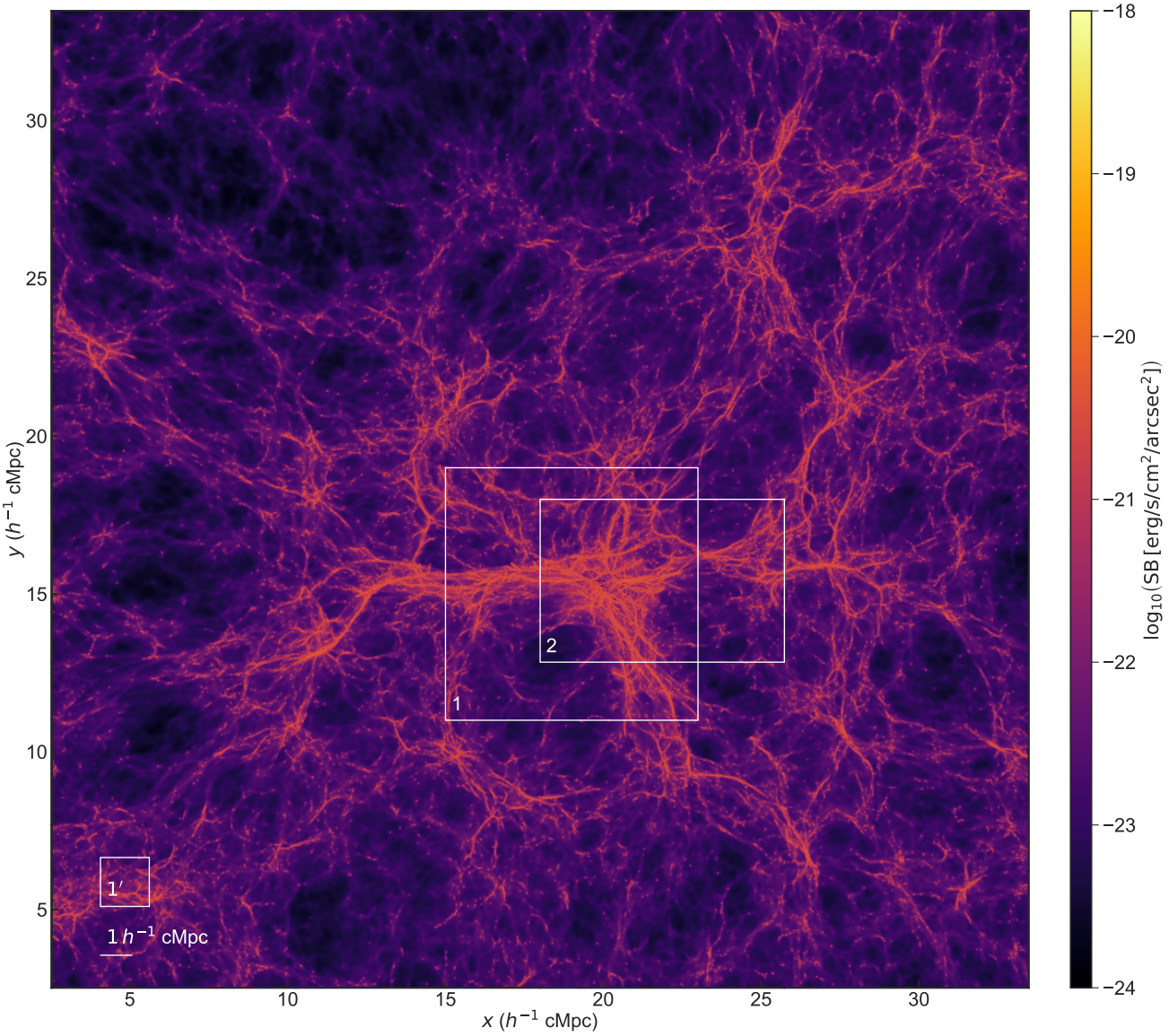

Fig. 4. Lyα SB resulting from the combination of recombination emission (of all gas in the simulation) below the mirror limit and collisional excitation of gas below half the critical self-shielding density, covering an area of 20×20 arcmin^2, or $31.0 \times 31.0\,h^{-2}$ cMpc^2, in a narrowband with $\Delta\lambda_{\rm obs} = 8.75$ Å (corresponding to $\sim 2.7\,h^{-1}$ cMpc) in a simulation snapshot at $z = 4.8$. The images are made by the projection method (Sect. 2.4.1) onto a pixel grid of 6000×6000; this is the same pixel size as MUSE, making this image the equivalent of a mosaic of 20×20 MUSE pointings (more details on MUSE follow in Sect. 3.3). Regions 1 and 2, indicated by the white rectangles, will be studied in more detail later. Also shown in the bottom left corner are the scales of the MUSE FOV (1×1 arcmin^2) and $1\,h^{-1}$ cMpc.

For collisional excitation, there should be two relevant effects: in the optically thin limit, the neutral fraction in ionisation equilibrium increases proportional to the density, hence $n_{\rm HI} \sim n_{\rm H}^2$; consequently, the emissivity scales as $\epsilon_{\rm exc} \sim n_{\rm HI} n_{\rm e} \sim n_{\rm H}^3$. If the emission were again produced at fixed overdensity, and if there is little evolution in the photoionisation rate, this would hence scale as

$$\epsilon_{\rm rec} \sim \Delta^3 (1+z)^9 (\text{physical luminosity density}) \text{ or} \quad (6)$$
$$\epsilon_{\rm rec} \sim \Delta^3 (1+z)^6 (\text{comoving luminosity density}),$$

where $\epsilon_{\rm exc}$ is the emissivity from collisional excitation. However, collisional excitation does not follow the predicted $(1+z)^6$ scaling in Eq. (6) (and hence is not shown), even decreasing with redshift at $z \gtrsim 3$. This suggests that it is dominated by emission near the critical self-shielding density (see also Sect. 3.2) and is hence more strongly affected by the density limit at half the critical self-shielding density, which decreases with increasing redshift more strongly than the mean density (i.e. the critical self-shielding overdensity decreases towards higher redshift, see Sect. 2.2.2). Still, we note that, depending on the precise distribution of self-shielded regions, which is dictated by local ionising sources on a small scale, collisional excitation from dense gas could account for an additional increase of the comoving luminosity density that surpasses the cosmic SB dimming effect, which itself scales as $(1+z)^4$.

3.2. Surface brightness maps

Fig. 4 shows a SB map that is the combination of recombination emission (of all gas in the simulation) below the mirror limit and collisional excitation of gas below half the critical self-shielding

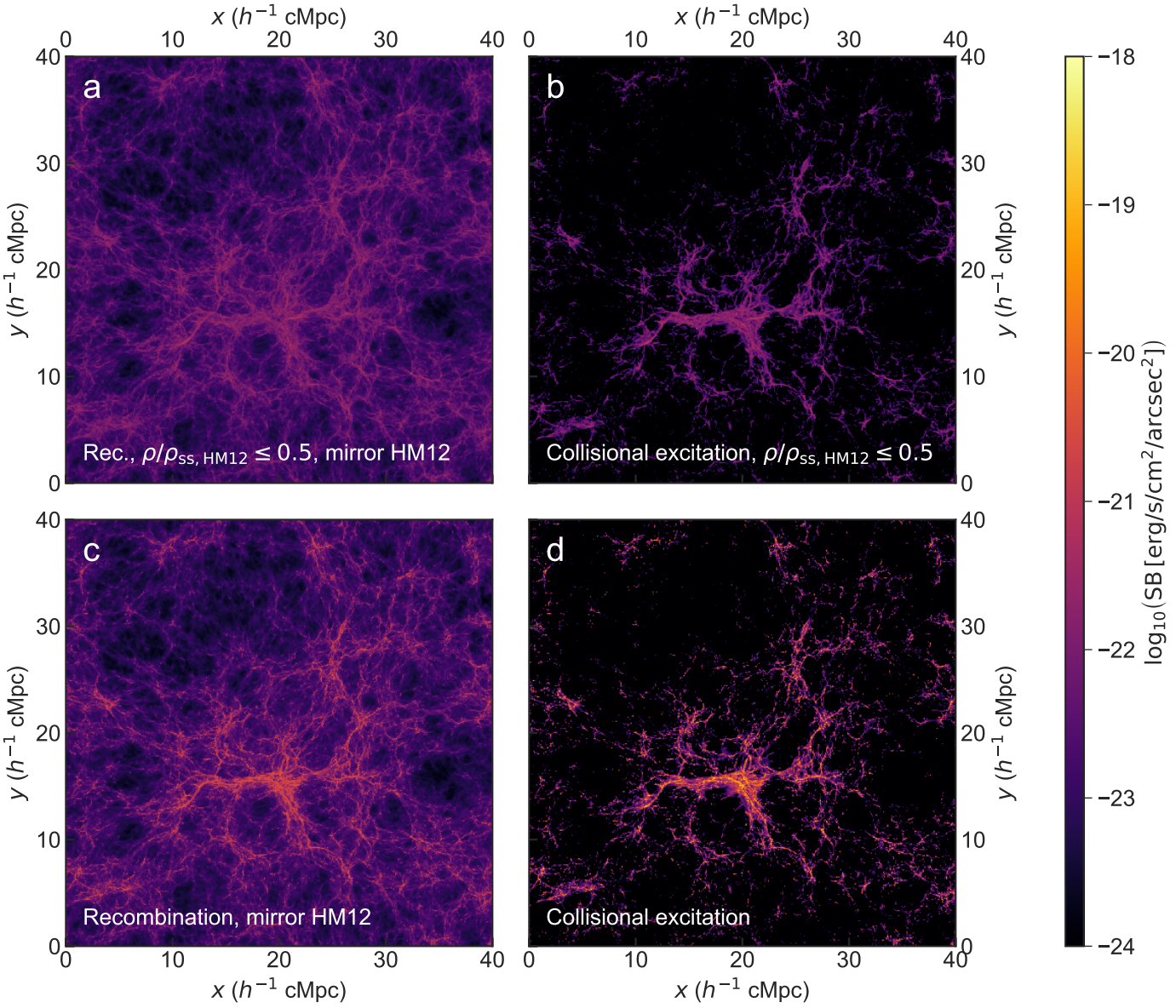

Fig. 5. Lyα SB of recombination (*panel a*) and collisional excitation (*panel b*) processes in a simulation snapshot at $z = 4.8$, for the gas at densities below half the critical self-shielding density in a narrowband with $\Delta\lambda_{\mathrm{obs}} = 8.75$ Å, or $\sim 2.7\,h^{-1}$ cMpc; the projections are made with pixel grid sizes of 1024×1024. These images show the entire (two-dimensional) spatial extent of the simulation, $40 \times 40\,h^{-2}$ cMpc^2 (25.8×25.8 arcmin^2). *Panels c and d*: same maps, but without a density cut-off.

density in a simulation snapshot at $z = 4.8$, for a narrowband with $\Delta\lambda_{\mathrm{obs}} = 8.75$ Å (at this redshift coinciding with a thickness of the slice of $\sim 2.7\,h^{-1}$ cMpc). The map shows a region corresponding to 20×20 arcmin^2. Also shown in the bottom left corner is the size of the MUSE field of view (FOV; 1×1 arcmin^2 – see Sect. 3.3 for more details). Regions 1 and 2, indicated by the white rectangles, will be studied in more detail later. The values of the SB for this narrowband width are of the order of SB $\lesssim 10^{-23}$ erg s^{-1} cm^{-2} arcsec^{-2} for the void regions, increasing to typically $\sim 10^{-21}$ erg s^{-1} cm^{-2} arcsec^{-2} for the IGM filaments. The denser regions have intensity peaks that typically show SB values of $\sim 10^{-20}$ erg s^{-1} cm^{-2} arcsec^{-2}.

Fig. 5 shows the same narrowband slice as in Fig. 4 (now for the full spatial extent of the simulation box, $40 \times 40\,h^{-2}$ cMpc^2 or 25.8×25.8 arcmin^2) split into contributions from recombination and collisional excitation processes in the gas. These maps were all made by projection onto a grid of 1024×1024 pixels. As before, a narrowband slice with $\Delta\lambda_{\mathrm{obs}} = 8.75$ Å ($\sim 2.7\,h^{-1}$ cMpc) was chosen. Panels a and b show gas at densities below half the critical self-shielding density, while panels c and d show all gas. The mirror limit was applied to both panels showing recombination emission (a and c). In this large-scale narrowband image, the total luminosity of recombination processes below half the critical self-shielding density – that is the total in panel a before imposing the mirror limit (although no pixels are in fact above the limit in this panel) – is $\sim 1.75 \cdot 10^{43}$ erg s^{-1}. For collisional excitation (the total in panel b), this is $\sim 5.45 \cdot 10^{42}$ erg s^{-1}. Including all gas, the total luminosity is $\sim 5.02 \cdot 10^{43}$ erg s^{-1} for recombination (panel c), again before imposing the mirror limit (now only 0.37% of pixels are above the limit); the total value is $\sim 2.21 \cdot 10^{44}$ erg s^{-1} for collisional excitations (panel d). We note that while collisional excitations dominate over recombinations

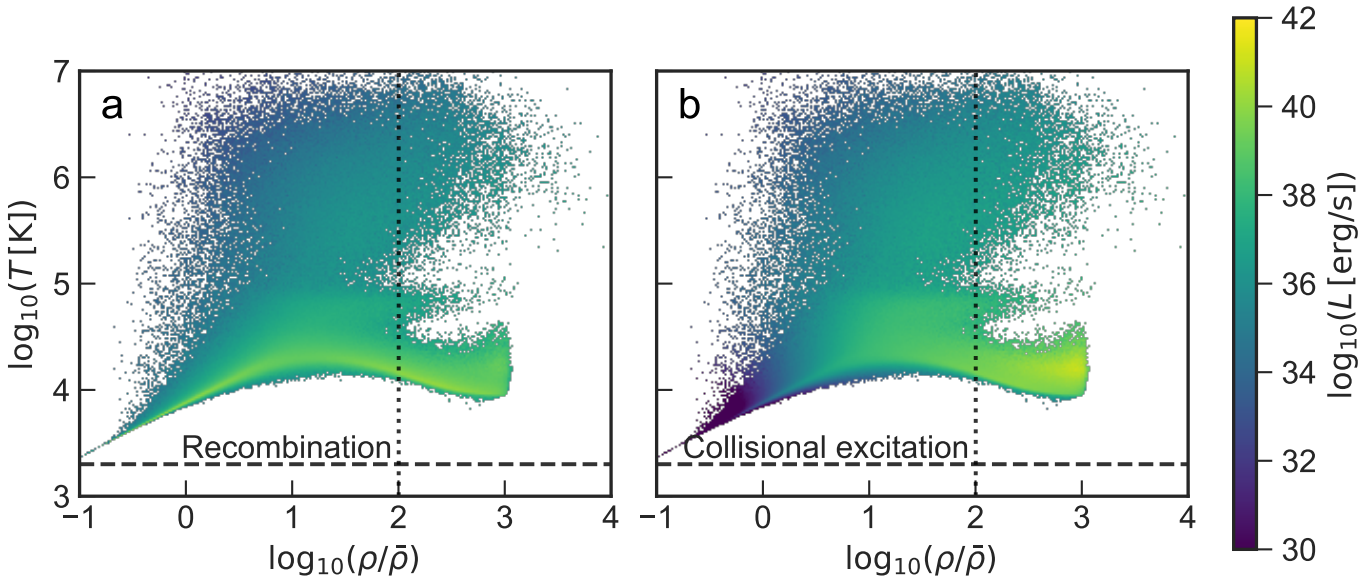

Fig. 6. Histogram of Lyα luminosities of recombination (*panel a*) and collisional excitation (*panel b*) processes in the same region as shown in Fig. 5 (a narrowband with $\Delta\lambda_{\mathrm{obs}} = 8.75$ Å, equivalent to $\sim 2.7\,h^{-1}$ cMpc) in a simulation snapshot at $z = 4.8$ in phase space. The colour represents the total luminosity in the simulation per histogram bin. The horizontal dashed line corresponds to the lower limit above which the fitting function of Scholz et al. (1990) and Scholz & Walters (1991) for collisionally excited Lyα emission is valid; the upper limit lies above the plotted range. The vertical dotted line shows the critical self-shielding density threshold at this redshift for the HM12 UVB (from Eq. (13) in Rahmati et al. 2013). Densities above the threshold are also more strongly affected by modelling uncertainties.

at high densities, the two processes contribute more equally at the lower densities prevalent in large-scale-structure filaments; recombination prevails slightly over collisional excitation below our adopted threshold. Moreover, gas near or somewhat above the critical self-shielding density contributes significantly to the maximum SB that is reached for both channels. We conclude that the recombination prediction including all gas while the mirror limit is imposed should yield at least a robust lower limit, while the collisional excitation prediction for gas at higher densities is more uncertain, thereby motivating our conservative density limit (Sect. 2.2.2).

While overall these SB maps exhibit the same structure as Fig. 4, the spatial distribution of emission coming from collisional and recombination processes is different. The degree of clustering in the emission is lower for the emission produced by recombination processes than it is for the contribution of collisional excitation. Recombination and collisional excitation depend differently on temperature and density, as discussed in Sect. 3.1. In particular, at fixed temperature and photoionisation rate, recombinations are proportional to the square of the density, $\sim\rho^2$, while in ionisation equilibrium collisional excitations are proportional to $\sim\rho^3$. As a consequence, recombinations are more equally spread across the volume, while collisional excitations are clearly more important at higher densities, thus reflecting the filamentary structure of the cosmic web better and leaving darker voids in between. To understand this in more detail, we now turn to the phase-space distribution of the gas in the simulation.

In Fig. 6, the luminosity in the simulation is shown at the same redshift and the same region as in Fig. 5 (also in the identical narrowband slice of $\Delta\lambda_{\mathrm{obs}} = 8.75$ Å, or $\sim 2.7\,h^{-1}$ cMpc), now as a luminosity-weighted, two-dimensional histogram in temperature and density. This illustrates what was discussed in Sect. 3.1 and shown in Fig. 5: collisional excitation is not effective at lower densities and the most luminous gas particles are located in the upper part of the very high-density cooling branch. Recombination emission, on the other hand, exhibits luminosities that are more comparable at lower and higher densities.

From the phase-space distribution in Fig. 6, it is clear that very little gas has temperatures outside of the temperature range of $2 \cdot 10^3\,\mathrm{K} \leq T \leq 1 \cdot 10^8\,\mathrm{K}$, for which our fitting function for collisionally excited Lyα is valid. The lower limit of this fitting function is indicated by the horizontal dashed line; the upper limit lies above the plotted range and almost all of the gas in the simulation[2]. The contribution from gas outside of this temperature range will be very small and we thus neglect it here.

The vertical dotted line shows the critical self-shielding density threshold at this redshift for the HM12 UVB (from Eq. (13) in Rahmati et al. 2013), illustrating the limiting density below which gas is not be strongly affected by the details of modelling self-shielding.

3.3. Observing facilities

In Table 1, an overview of a selection of current and future instruments that could potentially detect Lyα emission from IGM filaments is shown along with their wavelength and redshift range, FOV, and resolving power (R). Most ground- and space-based instruments that may be considered for detection of the diffuse IGM naturally observe in the visible spectrum and the ultraviolet, respectively, given the limitations of ground-based observations owing to absorption by Earth's atmosphere. This necessarily restricts the redshift range in which these instruments could observe Lyα. For ground-based observations, the typical redshift is $z \gtrsim 2.5$, whereas space-based telescopes observing in the UV can detect Lyα at lower redshifts. In principle, satellites carrying UV detectors could observe Lyα from $z \sim 0$ up to about $z \sim 1.5$.

IFU spectrographs arguably have the best instrument design for directly detecting emission from the cosmic web, owing to

[2] This is the case for the entire relevant redshift range.

Table 1. Overview of a selection of current and future instruments that might be most promising for detecting IGM filaments.

Name	Wavelength range λ (Å)	Redshift range $z_{\mathrm{Ly}\alpha}$	Field of view	Resolution R
Current IFU instrumentation				
KCWI-Blue (Keck)	3500–5600	1.9–3.6	20×33 arcsec^2	1000–20 000
MUSE (VLT)	4650–9300	2.8–6.7	1×1 arcmin^2	1770–3590
KMOS (VLT)	8000–25 000	5.6–19.6	65×43 arcsec	2000–4200
OSIRIS (Keck)	10 000–24 500	7.2–19.1	4.8×6.4 arcsec^2	2000–4000
SINFONI (VLT)	11 000–24 500	8.0–19.1	8×8 arcsec^2	2000–4000
Upcoming IFU instrumentation				
KCRM (KCWI-Red, Keck)	5300–10 500	3.4–7.6	20×33 arcsec^2	1000–20 000
HARMONI (ELT)	4700–24 500	2.9–19.1	6.4×9.1 arcsec^2	3000–20 000
BlueMUSE (VLT)	3500–6000	1.9–3.9	1.4×1.4 arcmin^2	~3000–5000
Upcoming and/or proposed space missions				
SPHEREx [(*)]	7500–50 000	5.2–40.1	3.5×11.3 deg^2	41–130
MESSIER [(*)]	~2000–7000	~0.5–4	2×2 deg^2	...
WSO-UV	1150–3200	~0–1.5	70×75 arcsec^2	~500

Notes. Fields left blank indicate currently unknown or undecided values. All current instruments presented are IFU spectrographs, upcoming and/or proposed instruments include several IFU spectrographs and space telescopes (two UV satellites and one IR spectrophotometer). Future experiments are in the development stage, unless marked with an asterisk. [(*)]Proposed space missions.

the flexibility in extracting pseudo-narrowband images over a wide range of bandwidths and central wavelengths and thereby resolving structures both spatially and spectrally over a large cosmic volume at once. The typical narrowband width extracted from IFU spectrographs to observe Lyα emission is <10 Å (e.g., Wisotzki et al. 2016, 2018). This value is almost an order of magnitude smaller than that obtained from photometric narrowband imaging with typical bandwidths of ~80–100 Å (Steidel et al. 2011; Ouchi et al. 2018). This significantly improves the contrast of IFU emission line maps for observations limited by sky noise. Despite the limited contrast for individual images, photometric narrowband studies still have detected large-scale Lyα emission in stacking analyses (e.g., Steidel et al. 2011; Matsuda et al. 2012; Kakuma et al. 2019), enabled by the wide FOV and large number of sources collected by such cameras. In particular, the recently installed Hyper Suprime-Cam on Subaru is currently obtaining 26 deg^2 narrowband imaging from redshift $z = 2.2$–6.6 as part of the Hyper Suprime-Cam Subaru Strategic Program (e.g., Ouchi et al. 2018). However, for this work, we focus on instruments that are most likely to obtain individual detections of Lyα emission from the cosmic web. Before the appearance of IFU imaging, another spectroscopic method used was long-slit spectroscopy (as in e.g., Rauch et al. 2008). But with the arrival of integral field spectroscopy, the volume probed by deep observations targeting Lyα emission could be dramatically increased, rendering long-slit spectroscopy a non-competitive alternative for this purpose.

The Very Large Telescope (VLT) has the widest range of IFU spectrographs. The current near-IR instruments at this facility are the Spectrograph for INtegral Field Observations in the Near Infrared (SINFONI, see Eisenhauer et al. 2003; Bonnet et al. 2004) and the *K*-band Multi Object Spectrograph (KMOS, see Sharples et al. 2013). Owing to their spectral range, these instruments are only able to observe Lyα at very high redshifts, respectively, $z > 8.0$ and $z > 5.6$, where the partly neutral IGM is expected to absorb most Lyα emission. The Multi Unit Spectroscopic Explorer (MUSE), an IFU spectrograph operating in the visible wavelength range (see Bacon et al. 2010), was most recently installed on the VLT. The combination of its relatively large FOV (1×1 arcmin^2) and spectral coverage (4650–9300 Å), while maintaining good spectral resolution (ranging between 1770–3590), currently makes this instrument one of the most promising candidates for the purpose of imaging the cosmic web in Lyα. BlueMUSE (Richard et al. 2019) is a proposed second MUSE instrument that will be optimised for the blue end of the visible wavelength range. Future instruments at the successor of the VLT, the ELT, include the High Angular Resolution Monolithic Optical and Near-infrared Integral field spectrograph (HARMONI, see Thatte et al. 2014), which is expected to be operational in 2025.

The blue channel of the Keck Cosmic Web Imager (KCWI, see Morrissey et al. 2018) is an instrument similar to VLT/MUSE at the Keck II telescope. This instrument offers a slightly better spectral sampling, although the FOV and spatial resolution are smaller and lower (20×33 arcsec^2 and 1.4 arcsec), respectively. However, since it has only become operational in 2018, no deep-field imaging such as the MUSE observations of the *Hubble* Deep Field South and *Hubble* Ultra-Deep Field (Bacon et al. 2015, 2017) has been released publicly yet. The red channel to KCWI, the Keck Cosmic Reionization Mapper (KCRM), is currently under construction and will complement the blue channel to cover the full wavelength range of 3500–10 500 Å ($3.4 < z_{\mathrm{Ly}\alpha} < 7.6$). Similar to SINFONI on the VLT, Keck currently has a near-infrared IFU spectrograph, OSIRIS. This instrument has a small FOV that can target Lyα only above $z > 7.2$, where the considerably neutral IGM is expected to absorb most emission.

For completeness, we also mention several promising space-based experiments: the World Space Observatory-Ultraviolet (WSO-UV, see Sachkov et al. 2018), and MESSIER (Valls-Gabaud & MESSIER Collaboration 2017), two proposed UV satellites. These satellites are proposed to have large FOVs and high sensitivities, but are limited to the lower redshift range ($z < 1.5$). In this work, we instead focus our attention on the high-redshift regime ($z > 3$). In February 2019, SPHEREx (Doré et al. 2018) was selected as the next

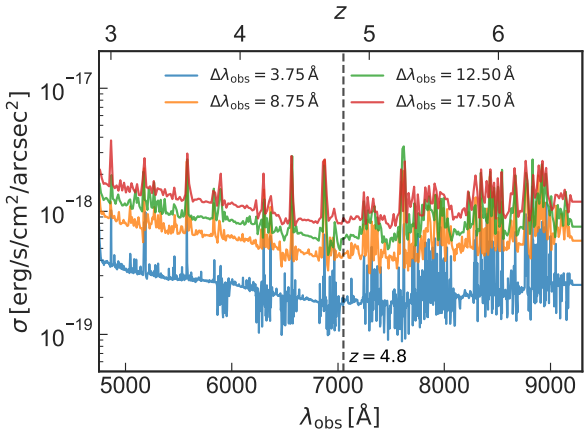

Fig. 7. Inferred noise in the MUSE HDFS observation as a function of observed wavelength or redshift for different pseudo-narrowband widths: $\Delta\lambda_{obs} = 3.75$ Å, $\Delta\lambda_{obs} = 8.75$ Å, $\Delta\lambda_{obs} = 12.50$ Å, and $\Delta\lambda_{obs} = 17.50$ Å. Skylines result in increased noise in some spectral ranges. The vertical dashed line indicates the position of Lyα at $z = 4.8$, which is located in a spectral window with lower noise. The throughput of MUSE is at its maximum of ∼40% at ∼7200 Å (e.g., Richard et al. 2019).

medium-class explorer mission by NASA and is targeted for launch in 2023. The SPHEREx mission will survey the entire sky with a spectrophotometer at very low spectral resolution, sensitive to diffuse Lyα emission at $z > 5.2$.

Out of the current instruments, MUSE arguably offers the best compromise of resolution, spectral coverage, and volume surveyed. The combination of its FOV of 1×1 arcmin^2 and spectral resolution make it a promising instrument to observe the cosmic web in Lyα emission. As a representative example of what has already been achieved, we now discuss in more detail the MUSE *Hubble* Deep Field South (HFDS; see Bacon et al. 2015). This is a 27 h integration of the HDFS, reaching a 1σ SB limit of $1 \cdot 10^{-19}$ erg s^{-1} cm^{-2} arcsec^{-2} for emission lines. In Fig. 7, we show the wavelength dependence of the inferred noise from the MUSE HDFS in pseudo-narrowbands of different widths for reference. We discuss the consideration of different narrowband widths in more detail in Sect. 3.4.1.

With MUSE, the Lyα emission can be observed over the redshift range of 2.8–6.7 (see Table 1). Hereafter, a redshift of $z = 4.8$ is specifically chosen for a more detailed study of our simulations. As already hinted at in Fig. 3, the diffuse gas in the IGM appears to be denser and potentially intrinsically more luminous in Lyα at higher redshifts; however, there are negating effects imposed by self-shielding because the critical self-shielding overdensity and the mirror limit steadily decrease towards higher redshifts (Sects. 2.1.2 and 2.2.2). We chose a redshift of 4.8 that seems to offer a reasonable compromise between these two effects, while also ensuring the results are not significantly affected by the details of feedback (Sect. 2.2.2). Finally, there is an additional component of emission from filaments due to halos and galaxies embedded within these filaments, the exact redshift dependence of which is difficult to predict. The following section describes more fully the outlook on observations of primarily the diffuse gas with a MUSE-like instrument. Specifically, we focus on such a wide-field integral field spectrograph on an ELT-class telescope to explore the most far-reaching observational prospects in the near future, discussing sensitivity limits, the overall redshift evolution, and optimal observing strategies.

To allow for a more realistic comparison between simulations and observations, some of the SB images hereafter (Figs. 9 and 10) are convolved with a Gaussian point spread function (PSF), to mimic the effect of seeing. The PSF full width at half maximum (FWHM) is chosen to be 0.75 arcsec, corresponding to the most conservative estimate for the MUSE HDFS (Bacon et al. 2015). In addition, these figures include noise that is added to the signal predicted from the simulations.

3.4. Simulated observations

3.4.1. Cosmic variance and narrowband widths

Before we look in more detail at observational strategies, we introduce two indicators of overdensity in the 'observed' simulation volume. The reason we introduce these specific characterisations of environment is to provide a quantitative way to distinguish different regions according to the level of their overall overdensity as could be characterised observationally. The first criterium to characterise environment, the baryonic overdensity, Δ_{baryon}, is computed by the ratio of baryonic density in the relevant region and the mean baryonic density at the redshift of the simulation. As a second criterion, we use the halo overdensity, Δ_{halo}, which is similar but instead of baryons uses halos with halo mass $M_h > 10^{9.5}\,M_\odot$: the amount of mass contained in these halos divided by the simulated (sub)volume as a fraction of their mean density, which is found by dividing the total mass of all halos with $M_h > 10^{9.5}\,M_\odot$ in the simulation box by its total volume[3]. This particular mass cut-off has been chosen as this is near the resolution limit of the simulation.

Now turning our attention to a MUSE-like instrument specifically, Fig. 8 shows several different SB images of the simulation at $z = 4.8$. The region of panel a has already been shown in Fig. 4 as region 1, while the other three images (panels b–d) are the angular size of 1×1 arcmin^2 and have a grid size of 300×300 pixels (corresponding to the FOV of the current MUSE instrument). In panels b–d, halos with halo mass of $M_h > 10^{9.5}\,M_\odot$ are shown as circles. Their size indicates their projected virial radii, $R_{vir,200}$, which is the radius within which their mass would result in a mean halo density of 200 times the mean density. Furthermore, the overdensity in each region shown is indicated in the bottom left corner of each panel in Fig. 8 according to the two different measures that have been introduced above.

Panels b–d show the signal as predicted from the simulation for three different 'IFU pointings'. The volume probed by each of these images at this redshift is $2.84\,h^{-3}$ cMpc^3. We note that we have chosen a smaller narrowband with $\Delta\lambda_{obs} = 3.75$ Å or $\sim 1.19\,h^{-1}$ cMpc at this redshift (equivalent to three spectral pixels of MUSE). Filamentary structures are still encapsulated in this width, while a smaller narrowband allows the signal to stand out more clearly from the noise: a wider narrowband, having more pixels in the spectral dimension, increases the overall noise level. The initial value of $\Delta\lambda_{obs} = 8.75$ Å, which we adopted from Wisotzki et al. (2016), was chosen for the observation of Lyα halos. Since Lyα scattering occurs increasingly in high-density regions and in the high-velocity outflowing gas near galaxies (e.g., Verhamme et al. 2006), these structures of

[3] Throughout this work, quoted halo masses are the dark matter mass of halos identified in the output snapshots of the simulation by a friends-of-friends algorithm with linking length 0.2, roughly corresponding to masses measured in spherical regions with a density of $\Delta = 200$ times the mean density of the Universe, that is M_{200m} (see e.g., Tinker et al. 2008).

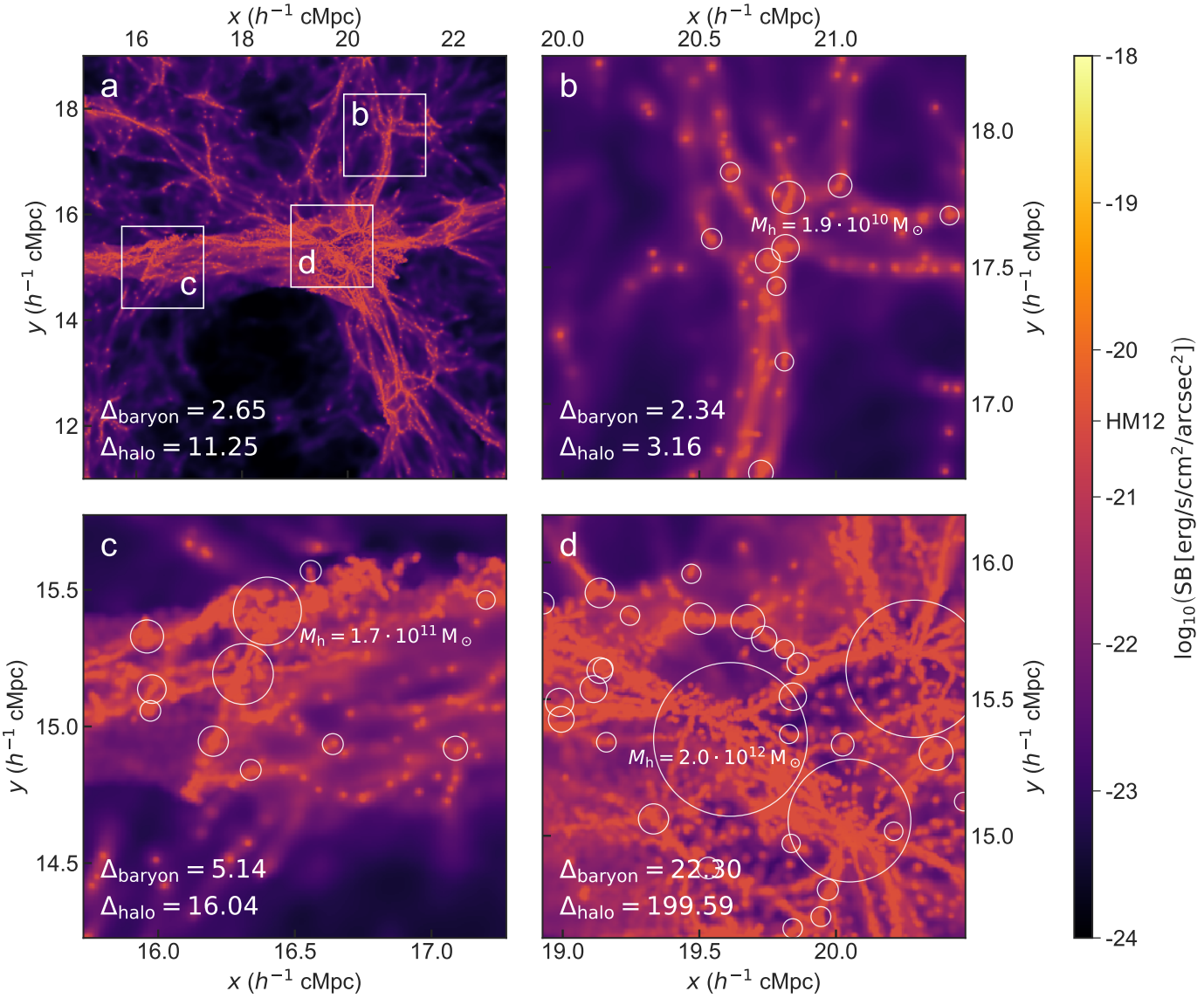

Fig. 8. Lyα SB for a narrowband with a smaller value of $\Delta\lambda_{\rm obs} = 3.75$ Å (i.e. $\sim 1.19\,h^{-1}$ cMpc) in a simulation snapshot at $z = 4.8$. As in Fig. 8, the SB shown is a combination of recombination emission (of all gas in the simulation) below the mirror limit (indicated on the colour bar as HM12), and collisional excitation of gas below half the critical self-shielding density. *Panel a*: overview narrowband image that corresponds to region 1 in Fig. 4. This is centred on the same comoving coordinates both spatially and spectrally, but now less extended in wavelength range as the narrowband width has been decreased. This panel shows a region of $8 \times 8\,h^{-2}$ cMpc^2 (5.2×5.2 arcmin^2) on a pixel grid of 1024×1024. *Panels b–d*: Lyα narrowband images the size of 1×1 arcmin^2 consisting of 300×300 pixels (as the FOV of MUSE). The volume probed by one of these narrowband images at this redshift is $2.84\,h^{-3}$ cMpc^3. The areas covered by these maps are indicated by the white squares in the overview panel a. Halos with halo mass of $M_{\rm h} > 10^{9.5}\,M_\odot$ are shown as circles, their size indicating their projected virial radius (see text). The most massive halo in each panel is annotated. In the bottom left corner of each panel, two different measures of the overdensity of the region are shown (see text for more details). The baryonic overdensity is calculated taking all gas into account, even though only gas below a certain density contributes to the collisional excitation.

high density and high gas velocities cause the Lyα signal to be spread out over a larger wavelength range.

Filamentary structures, however, have lower densities and peculiar velocities; hence, they are contained in a narrower wavelength range. Therefore, while on average more individual filaments are present when the chosen narrowband width is larger, the signal from a given filament tends to get lost in the noise, as illustrated by Fig. 7. Figure 8 indicates that individual filaments are still abundantly contained within these thin narrowband images with $\Delta\lambda_{\rm obs} = 3.75$ Å, which is getting near the limit of the typical spectral resolution ($\Delta\lambda \approx 2.5$ Å for MUSE, see Bacon et al. 2010). The precise spectral line width is determined by the details of radiative transfer, since Lyα photons are scattered away from the resonance frequency, depending on the kinematics of the scattering medium (see Appendix B); however, $\Delta\lambda_{\rm obs} = 3.75$ Å covers a velocity range of $\Delta v = 160\,{\rm km\,s^{-1}}$, which should be large enough to cover the line width for the modest optical depths in filaments (e.g., Eq. (21) in Dijkstra 2014).

As expected, regions with a higher signal (see two bottom panels in Fig. 8) contain more high-mass ($M_{\rm h} > 10^{9.5}\,M_\odot$) halos compared to low-density regions (e.g., panel b) and are found to have a higher overdensity, in both our proxies for

environment, $\Delta_{\rm baryon}$ and $\Delta_{\rm halo}$. The Lyα emission is mainly originating from in and around the virial radii of these halos, but filamentary structures can be seen to extend between them, up to comoving megaparsec scales in panel d. We note that the panel c and d are probably the optimal pointings in the entire region shown in panel a, indicating that with a randomly chosen field, there is only a rather modest chance of observing a filamentary structure with this relatively high SB. Figure 8 therefore highlights the importance of cosmic variance in detecting the filamentary structure of the IGM in Lyα emission. We conclude that both the instrument pointing and narrowband width chosen are essential to efficiently map the IGM in Lyα emission.

In practice, such overdensity candidates at $z \sim 4$ are readily identified at an on-sky number density of $\sim$1 deg^{-2} in broadband surveys (e.g., Toshikawa et al. 2016, 2018; the latter study identified $\sim$180 protocluster candidates over 121 deg^2 at $z \sim 4$). These still require spectroscopic follow-up observations of several individual member galaxies, however, to exclude the possibility of multiple overlapping structures in projection. The feasibility of such campaigns was for example demonstrated by Toshikawa et al. (2016). These authors confirm three out of four candidate protoclusters over a $\sim$4 deg^2 area at $z \sim 3$–4 (in excellent agreement with the expected fraction of true positives from cosmological simulations of more than 76%) using just over $\sim$1 h of spectroscopic observations with Subaru/FOCAS per protocluster candidate, thereby reaching a spectral resolution of $\Delta\lambda_{\rm obs} \sim 2.5$ Å.

We note that while a small narrowband width ($\Delta\lambda_{\rm obs} = 3.75$ Å or $\Delta z \sim 0.003$ as in Fig. 10) is optimal for a subsequent deep imaging campaign of extended, filamentary Lyα emission with a wide-field IFU, not all protocluster members necessarily need to be contained within such a narrow redshift range, since an IFU flexibly allows for the extraction of multiple pseudo-narrowbands along redshift space. Moreover, the IFU observation simultaneously provides the spectroscopic redshift of several galaxies in the protocluster through their Lyα emission or even fainter UV metal absorption or emission lines, if the exposure is sufficiently deep; this result can help guide the placement of such pseudo-narrowbands.

These recent studies furthermore give rise to a promising outlook for the search of protocluster candidates with extragalactic surveys in the near future. Just over two years into its main survey, the Vera Rubin Observatory has already reached a limiting i-band AB-magnitude of $\sim$26 (Ivezić et al. 2019), a depth similar to that of the survey used in Toshikawa et al. (2018), while the full 10-year survey (reaching 26.8 mag) will even approach the depth of the $\sim$4 deg^2 field considered by Toshikawa et al. (2016).

3.4.2. Sensitivity analysis

In Fig. 9, in all panels, a similar, small section of the main SB map at $z = 4.8$ (region 2 in Fig. 4) is shown in the same narrowband with $\Delta\lambda_{\rm obs} = 3.75$ Å (i.e. $\sim$1.19 h^{-1} cMpc), now with a Gaussian smoothing (FWHM of 0.75 arcsec). The columns show different assumptions on various limits (e.g., the signal from gas below 50 and 100 times the mean baryonic density, $\bar{\rho}$), while the overlaid Gaussian noise varies per row. Noise levels quoted are their values per pixel (before rebinning, discussed below). The pixels agree in size with those of MUSE (0.2 arcsec). Apart from the different gas density thresholds, the two columns on the right show the expectation in the mirror assumption, where, in addition to the collisional excitation luminosity of gas below a density of half the critical self-shielding density, we calculate the recombination luminosity arising from gas at all densities, but with the SB limited from above by the mirror value (see Sect. 2.1.2). At this redshift, the limit is equal to SB $\simeq 3.29 \cdot 10^{-21}$ erg s^{-1} cm^{-2} arcsec^{-2} for a HM12 UVB. Finally, the last column is rebinned on a scale of 10×10 pixels (2×2 arcsec^2) and subsequently convolved with a Gaussian with FWHM of equal size.

This particular region, chosen for its juxtaposition of both an under- and overdense region, shows that Lyα emission arising from the less dense components of filamentary structures can only be detected with very high sensitivities (of $\lesssim 10^{-20.5}$ erg s^{-1} cm^{-2} arcsec^{-2} for overdensities of $\rho/\bar{\rho} \leq 100$). Still, with image analysis techniques (e.g., rebinning pixels), the signal of these filaments can stand out at a noise level of $\sigma \sim 10^{-19.5}$ erg s^{-1} cm^{-2} arcsec^{-2}. Considering that the sensitivity in recent observations reaches a limiting SB of $\sim 10^{-19}$ erg s^{-1} cm^{-2} arcsec^{-2} (e.g., Bacon et al. 2015, 2017, 2021) or for median-stacked radial profiles even down to SB $\sim 4 \cdot 10^{-21}$ erg s^{-1} cm^{-2} arcsec^{-2} (or $\log_{10}$ SB $\simeq -20.4$; see Wisotzki et al. 2018), this suggests that the very deepest observations are getting close to the detection of such filamentary structures.

Returning to the region shown in panel d of Fig. 8, we construct mock observations for a MUSE-like, wide-field integral-field spectrograph on the ELT at two different redshifts, $z = 4.8$ and $z = 3.6$, in Fig. 10. The left panels show emission from all gas without any limits, while the right panels show the combination of recombination emission of all gas in the simulation below the mirror limit, and collisional excitation of gas below half the critical self-shielding density, as before. The panels on the right are convolved with a a Gaussian PSF corresponding to a FWHM of 0.75 arcsec (as in the HDFS observation, see Bacon et al. 2015) and include modelled noise. The noise level has been inferred from a continuum-subtracted pseudo-narrowband image (with the same width) constructed from the 27 h MUSE HDFS observation (Bacon et al. 2015) at $\sim$7200 Å, where the throughput of MUSE is at its maximum of $\sim$40% (e.g., Richard et al. 2019, ; but see also Fig. 7); the 1σ level of the inferred noise in this case is $\sigma = 1.72 \cdot 10^{-19}$ erg s^{-1} cm^{-2} arcsec^{-2}. Subsequently, the noise level is adjusted to correspond to a MUSE-like instrument on the ELT by scaling the sensitivity by the square root of the ratio of collecting areas between the VLT and ELT (52 m^2 and 978 m^2, respectively[4]) and an increased integration time of $t = 150$ h (again assuming a $1/\sqrt{N}$ scaling of the noise level with N the number of collected photons, resulting in a factor $\sqrt{150/27} \simeq 2.36$ lower noise in this case). The resulting noise level is $\sigma = 1.68 \cdot 10^{-20}$ erg s^{-1} cm^{-2} arcsec^{-2} (indicated on the colour bar).

There are two different evolutions in redshift at play in Fig. 10. First of all, we conclude that without conservative limits (not imposing the mirror limit and including gas at higher densities), the Lyα emission along filaments, originating from dense gas in halos and galaxies embedded in these filaments, is significantly brighter at higher redshift. This is clear from the comparison of the left panels between the two redshifts, $z = 4.8$ and $z = 3.6$ (panels a and c) and is an illustration of the cosmic density evolution winning over the increased SB dimming, as discussed in Sect. 3.1. The modelling of the dense gas dominating the emission is, however, very uncertain. A robust prediction can be obtained for low-density filamentary gas, for which we

[4] See for example https://www.eso.org/sci/facilities/paranal/telescopes/ut/m1unit.html and https://www.eso.org/public/teles-instr/elt/numbers/

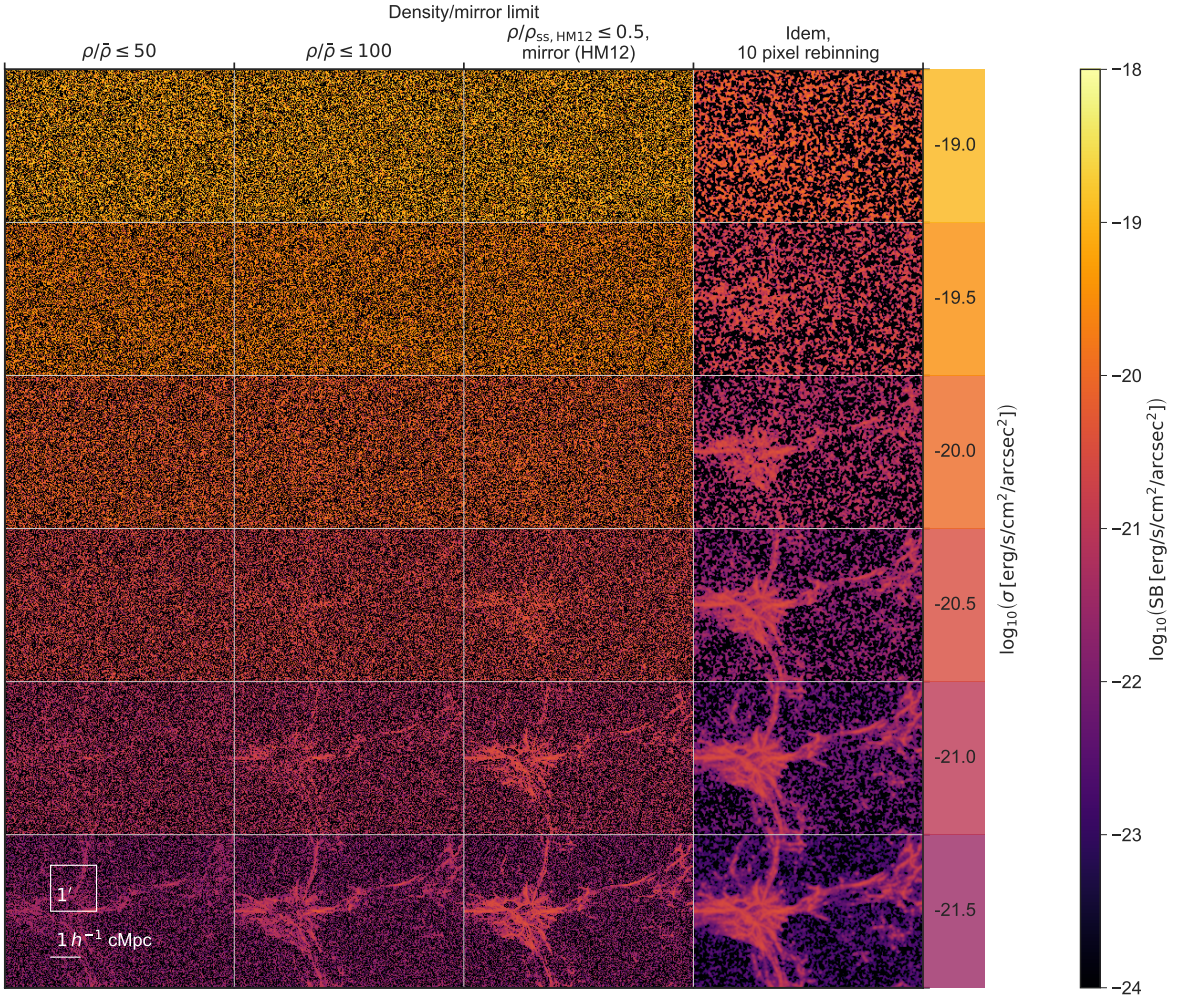

Fig. 9. Repeated view of region 2 of the $z = 4.8$ SB map in Fig. 4 for different noise levels and assumptions on various limits. The SB map has a narrowband with $\Delta\lambda_{\mathrm{obs}} = 3.75$ Å ($\sim$1.19 h^{-1} cMpc) and is convolved with a Gaussian kernel with a FWHM of 0.75 arcsec before adding noise (as in the HDFS observation, see Bacon et al. 2015). The spatial extent of each panel is 5×3.3 arcmin^2, or $7.8 \times 5.2\,h^{-2}$ cMpc^2. The 1σ levels of the Gaussian noise applied per pixel (before rebinning) to each panel in the entire row are indicated directly to the right of the mosaic, coloured according to the colour bar on the very right, while the density cut-off and mirror limit (if applied) for each column is shown above the mosaic (see text for details). The final column is identical to the column next to it, but has a smoothing of 10×10 pixels or 2×2 arcsec^2 applied (see text). Scales of 1×1 arcmin^2 (the MUSE FOV) and 1 h^{-1} cMpc are indicated on the bottom left. Each panel in the image has 1500×1000 pixels, again making the pixel size equal to that of MUSE (0.2 arcsec per pixel).

find that it can only be marginally detected in an extremely deep observation with an ELT-class telescope (panels b and d). In our most robust predictions, excluding emission from the dense (and complicated) central regions of halos, Lyα emission appears brighter at low redshift, where the mirror limit is less affected by SB dimming and self-shielding effects only start to play a role at higher overdensities (SB maps for a larger range of redshifts are shown in Appendix C). Future work that includes models with more detailed galaxy formation physics, simultaneously capturing the effects of self-shielding and baryonic feedback processes on high-density gas, is needed to investigate how precisely these two effects compete at different redshifts. An accurate treatment of the high-density gas is needed to point out the optimal redshift to observe gas in different environments.

4. Conclusions

We have presented simulation predictions on the properties of Lyα emission from low-density gas in the IGM at redshifts $2 < z < 7$. Based on our simulations we predict the Lyα emissivity due to recombinations and collisional excitations in the gas, carefully considering the relevant physical processes. We employed an on-the-fly self-shielding mechanism and neglected the effect of Lyα scattering, which is expected to be moderate in the low-density IGM. We impose the mirror limit for recombination emission and primarily focus on the regime that is not affected strongly by self-shielding for emission produced by collisional excitation by only considering gas that is well below the self-shielding critical density ($\rho/\bar{\rho} \sim 100$ at $z = 4.8$).

We found recombination to dominate at lower densities, while collisional excitation becomes the main emission process at higher densities. Recombination and collisional excitation contribute approximately equally for the regime we focus on, below half the self-shielding critical overdensity ($\rho/\bar{\rho} \lesssim 50$ at $z = 4.8$). Gas near or somewhat above the critical self-shielding density contributes significantly to luminosity produced through both channels. We show that our prediction of recombination emission including all gas, while having the mirror limit imposed, combined with collisional excitation emission

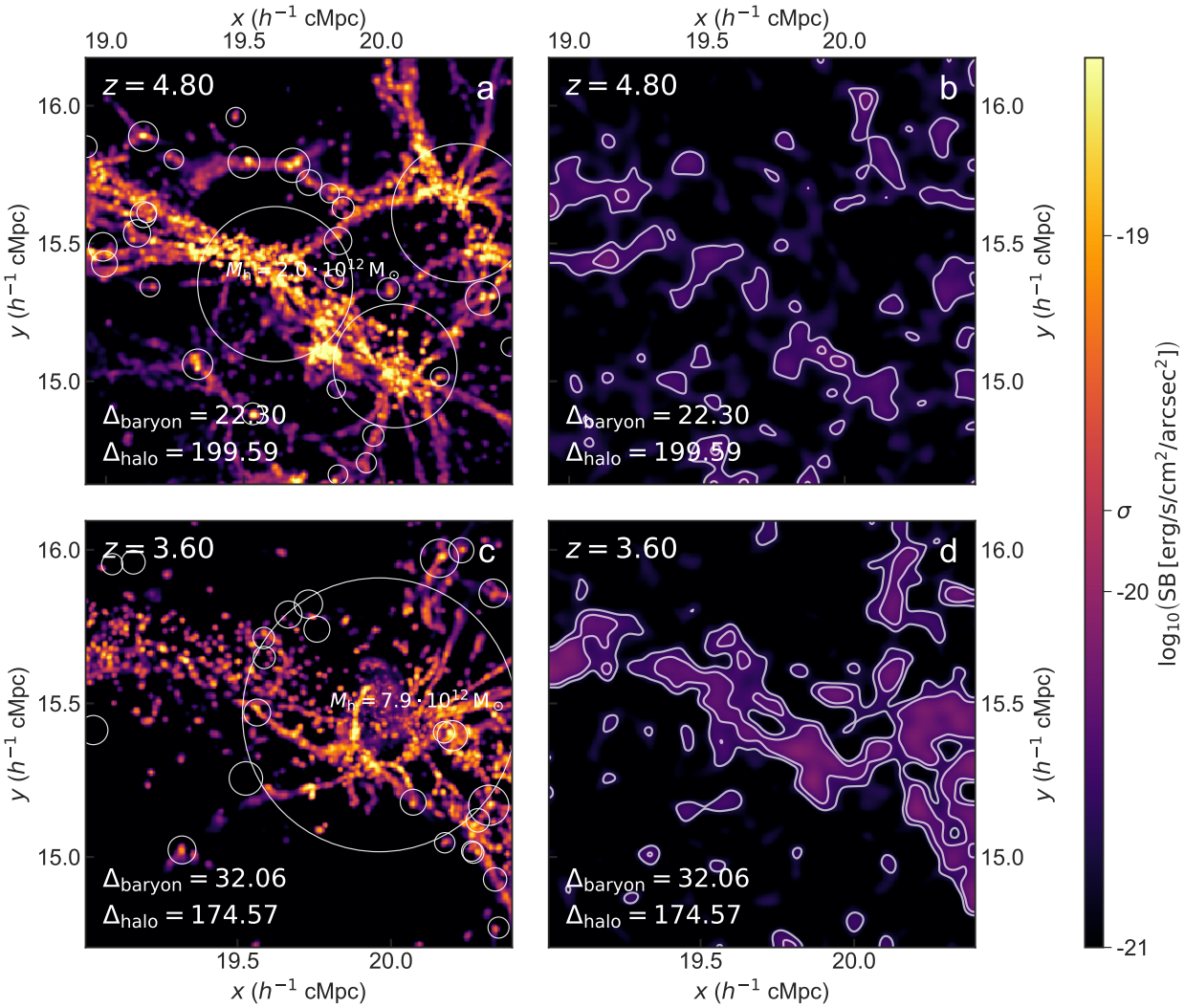

Fig. 10. Mock observations for a MUSE-like wide-field IFU instrument on the ELT covering the same region as panel d in Fig. 8 at two different redshifts ($z = 4.8$ and $z = 3.6$ on the top and bottom row, respectively) with no limits imposed and no observational effects vs. with mirror and density limits and modelled noise and seeing applied (left and right column, respectively; see text for details). The smaller narrowband with $\Delta\lambda_{\rm obs} = 3.75$ Å (i.e. $\sim 1.19\,h^{-1}$ cMpc) has been used again. These images have a different dynamical range than all other figures to accentuate the observable Lyα signal. In *panels b and d*, a rebinning of 10×10 pixels (2×2 arcsec^2) was applied, after which the image was smoothed on the same scale to recover the signal on larger scales. The white contours indicate measured 3σ and 5σ levels. The Lyα emission of IGM filaments can (marginally) be recovered in such an extremely deep observation and seems more feasible at low redshift when considering the robust lower limits (i.e. the mirror limit for recombinations and density threshold for collisional excitation; *panel d*); however, the predicted full intrinsic luminosity of filaments is notably higher at higher redshift (cf. *panels a and c*; see text for further discussion) but very dependent on the details of the modelling.

of low-density gas, should yield a robust lower limit. The prediction for Lyα emission of collisionally excited gas at higher densities is more uncertain, and we therefore leave this task to future work.

Our predicted values of the SB at $z = 4.8$ for narrowband images with $\Delta\lambda_{\rm obs} = 8.75$ Å are of the order of SB $\lesssim 10^{-23}$ erg s^{-1} cm^{-2} arcsec^{-2} for the void regions, increasing to $\sim 10^{-21}$ erg s^{-1} cm^{-2} arcsec^{-2} for the diffuse gas in filaments. Denser gas within (the halos of) galaxies embedded in the filaments can reach higher values and likely dominates the total emission from filaments. The modelling of this component is, however, very challenging as it depends on the details of the radiative transfer and feedback processes.

We briefly discussed the prospects of targeting diffuse Lyα emission with various spectrographs at different telescopes. At this moment, VLT/MUSE is arguably the best option for imaging the Lyα emission from gas in the filamentary structure of the cosmic web owing to its comparably large FOV (1×1 arcmin^2) and spectral coverage (4650–9300 Å, and thus accessible redshift range of 2.8–6.7 for Lyα), while maintaining a high spatial resolution (0.2 arcsec sampling) and good spectral resolution (ranging between 1770–3590). Recent deep observations reaching a limiting Lyα SB of $\sim 10^{-19}$ erg s^{-1} cm^{-2} arcsec^{-2} (e.g., Bacon et al. 2015, 2017, 2021), or for median-stacked radial profiles even down to SB $\sim 4 \cdot 10^{-21}$ erg s^{-1} cm^{-2} arcsec^{-2} (or $\log_{10}$ SB $\simeq -20.4$; see Wisotzki et al. 2018), suggest that the deepest current observations are already beginning to probe the extended Lyα radiation emitted by low-density gas ($\rho/\bar{\rho} \lesssim 100$) associated with filamentary structures; this observed emission, however, is likely dominated by dense gas in halos and galaxies embedded in them.

In our most conservative predictions, which should be considered as a lower limit, we exclude emission from the dense (and complicated) central regions of halos. In those predictions, the Lyα emission appears brighter at low redshift, where the mirror limit is less affected by SB dimming and self-shielding effects only start to play a role at relatively high overdensities. Our mock observations, which aim to simulate observations of regions at different overdensities, show a large amount of variance between fields. This variance makes densely populated protoclusters more promising targets for detecting the IGM in Lyα emission. Our findings suggest an observing strategy exploiting a targeted search of such a distant protocluster could potentially allow deep observations with a wide-field IFU instrument on an ELT-class telescope, a successor to MUSE, to directly map the intergalactic, low-density gas in Lyα emission in detail.

Acknowledgements. We are grateful to Sarah Bosman, Elisabeta Lusso, Michael Rauch, and Lutz Wisotzki for useful discussions regarding observational techniques and instruments, and to Lewis Weinberger for his contribution on the effects of radiative transfer. We furthermore thank the anonymous referee for their suggestions. EP acknowledges support by the Kavli Foundation. JW, EP, GK, and MGH gratefully acknowledge support from the ERC Advanced Grant 320596, "The Emergence of Structure During the Epoch of Reionization". JW and RS acknowledge support from the ERC Advanced Grant 695671, "QUENCH", and the Fondation MERAC. RS acknowledges support from an NWO Rubicon grant, project number 680-50-1518, and an STFC Ernest Rutherford Fellowship (ST/S004831/1). The Sherwood simulations were performed with supercomputer time awarded by the Partnership for Advanced Computing in Europe (PRACE) 8th Call. We acknowledge PRACE for awarding us access to the Curie supercomputer, based in France at the Très Grand Centre de Calcul (TGCC). This work also made use of the DiRAC Data Analytic system at the University of Cambridge, operated by the University of Cambridge High Performance Computing Service on behalf of the STFC DiRAC HPC Facility (www.dirac.ac.uk). This equipment was funded by BIS National E-infrastructure capital grant (ST/K001590/1), STFC capital grants ST/H008861/1 and ST/H00887X/1, and STFC DiRAC Operations grant ST/K00333X/1. DiRAC is part of the National e-Infrastructure. This work has also used the following packages in PYTHON: the SCIPY library (Jones et al. 2001), its packages NUMPY (van der Walt et al. 2011) and MATPLOTLIB (Hunter 2007), and the ASTROPY package (Astropy Collaboration 2013, 2018).

References

Arrigoni Battaia, F., Hennawi, J. F., Cantalupo, S., & Prochaska, J. X. 2016, ApJ, 829, 3
Arrigoni Battaia, F., Hennawi, J. F., Prochaska, J. X., et al. 2019, MNRAS, 482, 3162
Astropy Collaboration (Robitaille, T. P., et al.) 2013, A&A, 558, A33
Astropy Collaboration (Price-Whelan, A. M., et al.) 2018, AJ, 156, 123
Augustin, R., Quiret, S., Milliard, B., et al. 2019, MNRAS, 489, 2417
Bacon, R., Accardo, M., Adjali, L., et al. 2010, in Ground-based and Airborne Instrumentation for Astronomy III, eds. I. S. McLean, S. K. Ramsay, H. Takami, et al., SPIE Conf. Ser., 7735, 773508
Bacon, R., Brinchmann, J., Richard, J., et al. 2015, A&A, 575, A75
Bacon, R., Conseil, S., Mary, D., et al. 2017, A&A, 608, A1
Bacon, R., Mary, D., Garel, T., et al. 2021, A&A, 647, A107
Becker, G. D., & Bolton, J. S. 2013, MNRAS, 436, 1023
Becker, G. D., Bolton, J. S., Haehnelt, M. G., & Sargent, W. L. W. 2011, MNRAS, 410, 1096
Bolton, J. S., Becker, G. D., Raskutti, S., et al. 2012, MNRAS, 419, 2880
Bolton, J. S., Puchwein, E., Sijacki, D., et al. 2017, MNRAS, 464, 897
Bonnet, H., Abuter, R., Baker, A., et al. 2004, Messenger, 117, 17
Borisova, E., Cantalupo, S., Lilly, S. J., et al. 2016, ApJ, 831, 39
Cai, Z., Fan, X., Yang, Y., et al. 2017, ApJ, 837, 71
Cantalupo, S. 2017, in Gas Accretion and Giant Lyα Nebulae, eds. A. Fox, & R. Davé (Springer International Publishing AG), 430, 195
Cantalupo, S., Porciani, C., Lilly, S. J., & Miniati, F. 2005, ApJ, 628, 61
Cantalupo, S., Porciani, C., & Lilly, S. J. 2008, ApJ, 672, 48
Cantalupo, S., Lilly, S. J., & Haehnelt, M. G. 2012, MNRAS, 425, 1992
Cantalupo, S., Arrigoni-Battaia, F., Prochaska, J. X., Hennawi, J. F., & Madau, P. 2014, Nature, 506, 63
Cen, R., Miralda-Escudé, J., Ostriker, J. P., & Rauch, M. 1994, ApJ, 437, L9
Chiang, Y.-K., Ménard, B., & Schiminovich, D. 2019, ApJ, 877, 150
Cisewski, J., Croft, R. A. C., Freeman, P. E., et al. 2014, MNRAS, 440, 2599
Croft, R. A. C., Miralda-Escudé, J., Zheng, Z., Blomqvist, M., & Pieri, M. 2018, MNRAS, 481, 1320
Davé, R., Hernquist, L., Katz, N., & Weinberg, D. H. 1999, ApJ, 511, 521
de Graaff, A., Cai, Y.-C., Heymans, C., & Peacock, J. A. 2019, A&A, 624, A48
Dijkstra, M. 2014, PASA, 31
Djorgovski, S., Spinrad, H., McCarthy, P., & Strauss, M. A. 1985, ApJ, 299, L1
Doré, O., Werner, M. W., Ashby, M. L. N., et al. 2018, ArXiv e-prints [arXiv:1805.05489]
Draine, B. T. 2011, Physics of the Interstellar and Intergalactic Medium (Princeton University Press)
Eckert, D., Jauzac, M., Shan, H., et al. 2015, Nature, 528, 105
Eisenhauer, F., Abuter, R., Bickert, K., et al. 2003, in Instrument Design and Performance for Optical/Infrared Ground-based Telescopes, eds. M. Iye, A. F. M. Moorwood, et al., SPIE Conf. Ser., 4841, 1548
Elias, L. M., Genel, S., Sternberg, A., et al. 2020, MNRAS, 494, 5439
Fardal, M. A., Katz, N., Gardner, J. P., et al. 2001, ApJ, 562, 605
Faucher-Giguère, C.-A., Lidz, A., Hernquist, L., & Zaldarriaga, M. 2008, ApJ, 688, 85
Faucher-Giguère, C.-A., Kereš, D., Dijkstra, M., Hernquist, L., & Zaldarriaga, M. 2010, ApJ, 725, 633
Francis, P. J., Woodgate, B. E., Warren, S. J., et al. 1996, ApJ, 457, 490
Fumagalli, M., Cantalupo, S., Dekel, A., et al. 2016, MNRAS, 462, 1978
Furlanetto, S. R., Schaye, J., Springel, V., & Hernquist, L. 2003, ApJ, 599, L1
Furlanetto, S. R., Schaye, J., Springel, V., & Hernquist, L. 2005, ApJ, 622, 7
Fynbo, J. U., Møller, P., & Warren, S. J. 1999, MNRAS, 305, 849
Gallego, S. G., Cantalupo, S., Lilly, S., et al. 2018, MNRAS, 475, 3854
Garzilli, A., Boyarsky, A., & Ruchayskiy, O. 2017, Phys. Lett. B, 773, 258
Geach, J. E., Narayanan, D., Matsuda, Y., et al. 2016, ApJ, 832, 37
Gould, A., & Weinberg, D. H. 1996, ApJ, 468, 462
Haardt, F., & Madau, P. 2012, ApJ, 746, 125 (HM12)
Hayashino, T., Matsuda, Y., Tamura, H., et al. 2004, AJ, 128, 2073
Heckman, T. M., Lehnert, M. D., van Breugel, W., & Miley, G. K. 1991, ApJ, 370, 78
Heneka, C., Cooray, A., & Feng, C. 2017, ApJ, 848, 52
Hennawi, J. F., Prochaska, J. X., Cantalupo, S., & Arrigoni-Battaia, F. 2015, Science, 348, 779
Hernquist, L., Katz, N., Weinberg, D. H., & Miralda-Escudé, J. 1996, ApJ, 457, L51
Hogan, C. J., & Weymann, R. J. 1987, MNRAS, 225, 1P
Hu, E. M., Songaila, A., Cowie, L. L., & Stockton, A. 1991, ApJ, 368, 28
Humphrey, A., Villar-Martín, M., Sánchez, S. F., et al. 2008, MNRAS, 390, 1505
Hunter, J. D. 2007, Comput. Sci. Eng., 9, 90
Ikeuchi, S., & Ostriker, J. P. 1986, ApJ, 301, 522
Ivezić, Ž., Kahn, S. M., Tyson, J. A., et al. 2019, ApJ, 873, 111
Jones, E., Oliphant, T., Peterson, P., et al. 2001, SciPy: Open source scientific tools for Python
Kakuma, R., Ouchi, M., Harikane, Y., et al. 2019, ArXiv e-prints [arXiv:1906.00173]
Katz, N., Weinberg, D. H., & Hernquist, L. 1996, ApJS, 105, 19
Keel, W. C., Cohen, S. H., Windhorst, R. A., & Waddington, I. 1999, AJ, 118, 2547
Khaire, V., Walther, M., Hennawi, J. F., et al. 2019, MNRAS, 486, 769
Kollmeier, J. A., Zheng, Z., Davé, R., et al. 2010, ApJ, 708, 1048
Kulkarni, G., Worseck, G., & Hennawi, J. F. 2019a, MNRAS, 488, 1035
Kulkarni, G., Keating, L. C., Haehnelt, M. G., et al. 2019b, MNRAS, 485, L24
Kull, A., & Böhringer, H. 1999, A&A, 341, 23
Leclercq, F., Bacon, R., Wisotzki, L., et al. 2017, A&A, 608, A8
Lukić, Z., Stark, C. W., Nugent, P., et al. 2015, MNRAS, 446, 3697
Lusso, E., Fumagalli, M., Fossati, M., et al. 2019, MNRAS, 485, L62
Martin, D. C., Chang, D., Matuszewski, M., et al. 2014, ApJ, 786, 106
Matsuda, Y., Yamada, T., Hayashino, T., et al. 2012, MNRAS, 425, 878
McCarthy, P. J., Spinrad, H., van Breugel, W., et al. 1990, ApJ, 365, 487
Meiksin, A. A. 2009, Rev. Mod. Phys., 81, 1405
Meiksin, A., & White, M. 2003, MNRAS, 342, 1205
Momose, R., Ouchi, M., Nakajima, K., et al. 2014, MNRAS, 442, 110
Morrissey, P., Matuszewski, M., Martin, D. C., et al. 2018, ApJ, 864, 93
Oñorbe, J., Hennawi, J. F., & Lukić, Z. 2017, ApJ, 837, 106
Oñorbe, J., Davies, F. B., Lukić, Z., et al. 2019, MNRAS, 486, 4075
Oteo, I., Ivison, R. J., Dunne, L., et al. 2018, ApJ, 856, 72
Ouchi, M., Harikane, Y., Shibuya, T., et al. 2018, PASJ, 70, S13
Partridge, R. B., & Peebles, P. J. E. 1967, ApJ, 147, 868
Planck Collaboration XVI, 2014, A&A, 571, A16
Prescott, M. K. M., Dey, A., & Jannuzi, B. T. 2013, ApJ, 762, 38
Puchwein, E., Haardt, F., Haehnelt, M. G., & Madau, P. 2019, MNRAS, 485, 47 (P19)
Rahmati, A., Pawlik, A. H., Raičević, M., & Schaye, J. 2013, MNRAS, 430, 2427

Rauch, M., Miralda-Escudé, J., Sargent, W. L. W., et al. 1997, ApJ, 489, 7
Rauch, M., Haehnelt, M., Bunker, A., et al. 2008, ApJ, 681, 856
Rauch, M., Becker, G. D., Haehnelt, M. G., et al. 2011, MNRAS, 418, 1115
Rauch, M., Becker, G. D., Haehnelt, M. G., Gauthier, J.-R., & Sargent, W. L. W. 2013, MNRAS, 429, 429
Richard, J., Bacon, R., Blaizot, J., et al. 2019, ArXiv e-prints [arXiv:1906.01657]
Roche, N., Humphrey, A., & Binette, L. 2014, MNRAS, 443, 3795
Rosdahl, J., & Blaizot, J. 2012, MNRAS, 423, 344
Sachkov, M., Shustov, B., & Gómez de Castro, A. I. 2018, in Space Telescopes and Instrumentation 2018: Ultraviolet to Gamma Ray, eds. J. W. A. den Herder, S. Nikzad, & K. Nakazawa, SPIE Conf. Ser., 10699, 106993G
Sánchez, S. F., & Humphrey, A. 2009, A&A, 495, 471
Schaye, J., Theuns, T., Rauch, M., Efstathiou, G., & Sargent, W. L. W. 2000, MNRAS, 318, 817
Scholz, T. T., & Walters, H. R. J. 1991, ApJ, 380, 302
Scholz, T. T., Walters, H. R. J., Burke, P. J., & Scott, M. P. 1990, MNRAS, 242, 692
Sharples, R., Bender, R., Agudo Berbel, A., et al. 2013, Messenger, 151, 21
Silva, M. B., Kooistra, R., & Zaroubi, S. 2016, MNRAS, 462, 1961
Silva, M. B., Santos, M. G., Gong, Y., Cooray, A., & Bock, J. 2013, ApJ, 763, 132
Sobral, D., Smail, I., Best, P. N., et al. 2013, MNRAS, 428, 1128
Springel, V. 2005, MNRAS, 364, 1105
Springel, V., Yoshida, N., & White, S. D. M. 2001, New A, 6, 79
Steidel, C. C., Adelberger, K. L., Shapley, A. E., et al. 2000, ApJ, 532, 170
Steidel, C. C., Bogosavljević, M., Shapley, A. E., et al. 2011, ApJ, 736, 160
Tanimura, H., Hinshaw, G., McCarthy, I. G., et al. 2019, MNRAS, 483, 223
Thatte, N. A., Clarke, F., Bryson, I., et al. 2014, in Ground-based and Airborne Instrumentation for Astronomy V, eds. S. K. Ramsay, I. S. McLean, H. Takami, et al., SPIE Conf. Ser., 9147, 914725
Tinker, J., Kravtsov, A. V., Klypin, A., et al. 2008, ApJ, 688, 709
Toshikawa, J., Kashikawa, N., Overzier, R., et al. 2016, ApJ, 826, 114
Toshikawa, J., Uchiyama, H., Kashikawa, N., et al. 2018, PASJ, 70, S12
Umehata, H., Fumagalli, M., Smail, I., et al. 2019, Science, 366, 97
Valls-Gabaud, D., MESSIER Collaboration 2017, in Formation and Evolution of Galaxy Outskirts, eds. A. Gil de Paz, J. H. Knapen, & J. C. Lee, 321, 199
van der Walt, S., Colbert, S. C., & Varoquaux, G. 2011, Comput. Sci. Eng., 13, 22
Vanzella, E., Balestra, I., Gronke, M., et al. 2017, MNRAS, 465, 3803
Venemans, B. P., Röttgering, H. J. A., Miley, G. K., et al. 2007, A&A, 461, 823
Verhamme, A., Schaerer, D., & Maselli, A. 2006, A&A, 460, 397
Viel, M., Haehnelt, M. G., & Springel, V. 2004, MNRAS, 354, 684
Villar-Martín, M., Sánchez, S. F., Humphrey, A., et al. 2007, MNRAS, 378, 416
Walther, M., Oñorbe, J., Hennawi, J. F., & Lukić, Z. 2019, ApJ, 872, 13
Weinberg, D. H., Burles, S., Croft, R. A. C., et al. 1999, in Evolution of Large Scale Structure : From Recombination to Garching, eds. A. J. Banday, R. K. Sheth, L. N. da Costa, et al., 346
Wisotzki, L., Bacon, R., Blaizot, J., et al. 2016, A&A, 587, A98
Wisotzki, L., Bacon, R., Brinchmann, J., et al. 2018, Nature, 562, 229
Wold, I. G. B., Finkelstein, S. L., Barger, A. J., Cowie, L. L., & Rosenwasser, B. 2017, ApJ, 848, 108

Appendix A: Model parameters and fitting functions

Emission processes

This section contains the fitting functions for the relevant quantities in the formulae for recombination and collisional excitation emissivity (Eqs. (1) and (2) in Sects. 2.1 and 2.2), which are repeated here for clarity.
Recombination emissivity (Eq. (1)) is written as

$$\epsilon_{\rm rec}(T) = f_{\rm rec,A/B}(T)\, n_{\rm e}\, n_{\rm HII}\, \alpha_{\rm A/B}(T)\, E_{\rm Ly\alpha}. \tag{A.1}$$

Collisional excitation emissivity (Eq. (2)) is given by

$$\epsilon_{\rm exc}(T) = \gamma_{\rm 1s2p}(T)\, n_{\rm e}\, n_{\rm HI}\, E_{\rm Ly\alpha}. \tag{A.2}$$

Recombination fitting functions

The underlying equation governing Lyα emission due to recombination in the IGM is given in Eq. (A.1). The recombination fraction $f_{\rm rec,A/B}$ gives the number of recombinations that ultimately result in the emission of a Lyα photon. This fraction can be modelled using the relations given in Cantalupo et al. (2008) and Dijkstra (2014) and can be summarised as follows:

$$f_{\rm rec,A/B} = \begin{cases} 0.41 - 0.165 \log_{10}\left(\frac{T}{10^4\,\rm K}\right) - 0.015 \left(\frac{T}{10^4\,\rm K}\right)^{-0.44}, & \text{case-A} \\ 0.686 - 0.106 \log_{10}\left(\frac{T}{10^4\,\rm K}\right) - 0.009 \left(\frac{T}{10^4\,\rm K}\right)^{-0.44}, & \text{case-B.} \end{cases}$$

The recombination coefficient, $\alpha_{\rm A/B}$, is given in the work of Draine (2011) as follows:

$$\alpha_{\rm A/B} = \begin{cases} 4.13 \cdot 10^{-13} \left(\frac{T}{10^4\,\rm K}\right)^{-0.7131 - 0.0115 \log_{10}\left(\frac{T}{10^4\,\rm K}\right)}\ \rm cm^3\ s^{-1}, & \text{case-A} \\ 2.54 \cdot 10^{-13} \left(\frac{T}{10^4\,\rm K}\right)^{-0.8163 - 0.0208 \log_{10}\left(\frac{T}{10^4\,\rm K}\right)}\ \rm cm^3\ s^{-1}, & \text{case-B.} \end{cases}$$

Collisional excitation fitting functions

For collisional excitation, the Lyα luminosity density is given by Eq. (A.2). The function $\gamma_{\rm 1s2p}$ in this formula is given by

$$\gamma_{\rm 1s2p}(T) = \Gamma(T) \exp\left(-\frac{E_{\rm Ly\alpha}}{k_{\rm B} T}\right), \tag{A.3}$$

where $k_{\rm B}$ is the Boltzmann constant. The function $\Gamma(T)$ is characterised in Scholz et al. (1990) and Scholz & Walters (1991) as follows:

Table A.1. Coefficients c_i in Eq. (A.4) and their corresponding temperature regimes.

	Regime 1	Regime 2	Regime 3
c_0	$-1.630155 \cdot 10^2$	$5.279996 \cdot 10^2$	$-2.8133632 \cdot 10^3$
c_1	$8.795711 \cdot 10^1$	$-1.939399 \cdot 10^2$	$8.1509685 \cdot 10^2$
c_2	$-2.057117 \cdot 10^1$	$2.718982 \cdot 10^1$	$-9.4418414 \cdot 10^1$
c_3	2.359573	−1.883399	5.4280565
c_4	$-1.339059 \cdot 10^{-1}$	$6.462462 \cdot 10^{-2}$	$-1.5467120 \cdot 10^{-1}$
c_5	$3.021507 \cdot 10^{-3}$	$-8.811076 \cdot 10^{-4}$	$1.7439112 \cdot 10^{-3}$
	Regimes	Temperature values	
	Regime 1	$2 \cdot 10^3\ \rm K \leq T < 6 \cdot 10^4\ K$	
	Regime 2	$6 \cdot 10^4\ \rm K \leq T < 6 \cdot 10^6\ K$	
	Regime 3	$6 \cdot 10^6\ \rm K \leq T \leq 1 \cdot 10^8\ K$	

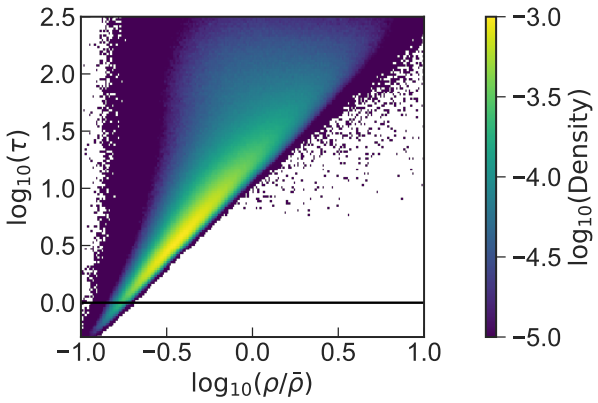

Fig. A.1. Two-dimensional density histogram for each of 2048 pixels in spectra along 5000 (randomly selected) lines of sight at $z = 4.8$, as a function of the Lyα optical depth τ and overdensity $\rho/\bar{\rho}$ in the sightline; the two parameters are measured at line centre, where the optical depth was divided by 2 just to account for the hydrogen between the source and the observer (see text).

$$\Gamma(T) = \exp\left(\sum_{i=0}^{5} c_i\, (\ln T)^i\right), \tag{A.4}$$

where the coefficients c_i found by Scholz et al. (1990) and Scholz & Walters (1991) are dependent on the temperature regime (shown in Table A.1). As noted in Sect. 2.2.1, the rates are not identical to those applied in the cosmological hydrodynamical simulation, but in the relevant temperature regime deviate so little that the Lyα emission would not be appreciably changed.

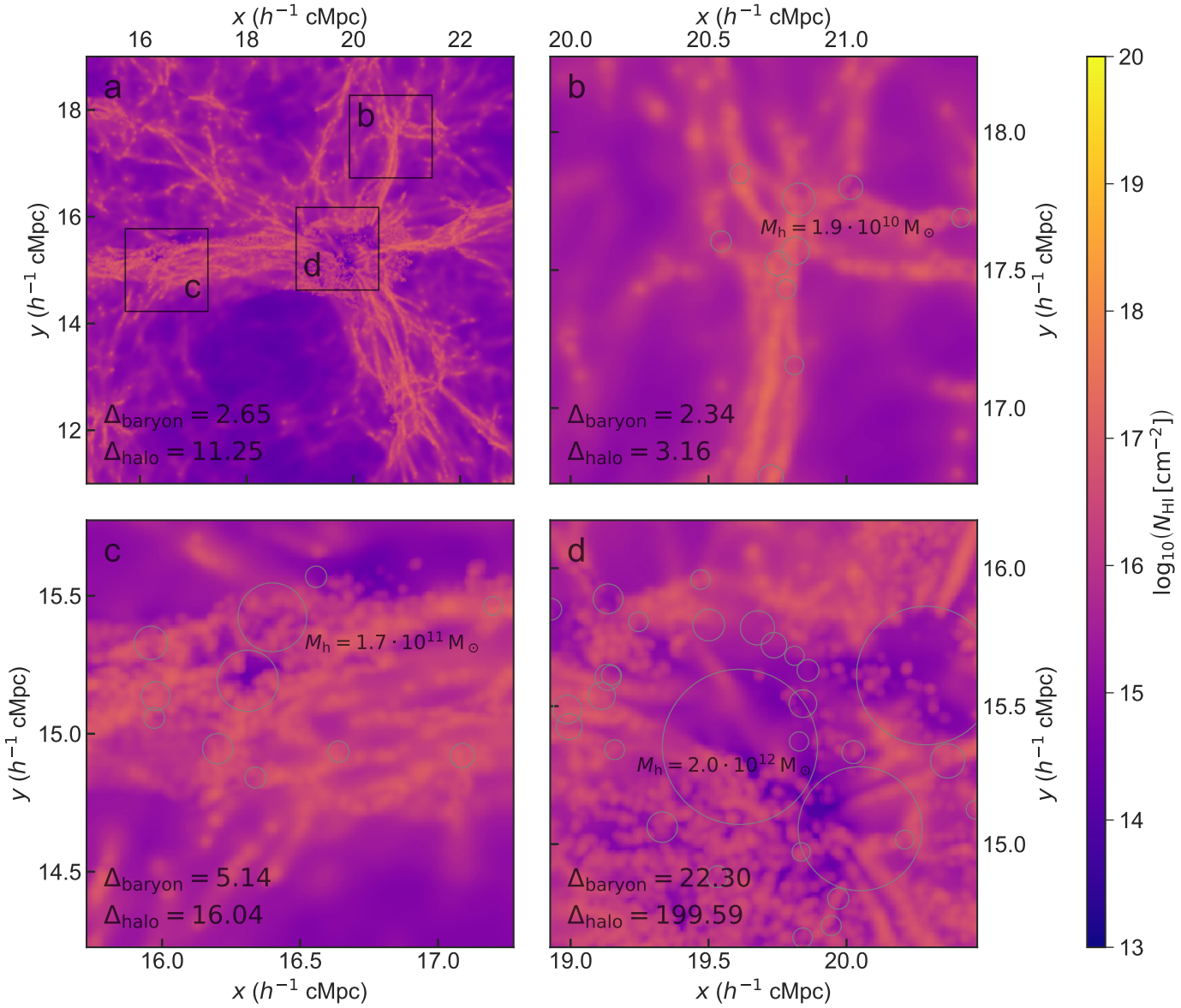

Fig. A.2. Simulated column density of neutral hydrogen, $N_{\rm HI}$, in a simulation snapshot at $z = 4.8$. The same regions as in Fig. 8 are shown. Moreover, the same density thresholds used for the collisional excitation component are applied, that is only gas below half the critical self-shielding density is shown, meaning this is the column density that would correspond to a narrowband image of the low-density gas with $\Delta\lambda_{\rm obs} = 3.75$ Å (~$1.19\,h^{-1}$ cMpc). *Panel a*: overview of part of the simulation snapshot that corresponds to region 1 in Fig. 4. This is centred on the same comoving coordinates both spatially and spectrally, but now less extended in wavelength range. This panel shows a region of $8 \times 8\,h^{-2}$ cMpc^2 (5.2×5.2 arcmin^2) on a pixel grid of 1024×1024. *Panels b–d*: column density maps of neutral hydrogen the size of the MUSE FOV consisting of 300×300 pixels. The areas covered by these maps are indicated by the black squares in the overview *panel a*. In the bottom left corner of each panel, two different measures of the overdensity of the region are shown (see Sect. 3.4 for more details). In *panels b–d*, halos with halo mass of $M_{\rm h} > 10^{9.5}\,M_\odot$ are shown as circles, their size indicating their projected virial radius (see Sect. 3.4). The most massive halo in each panel is annotated.

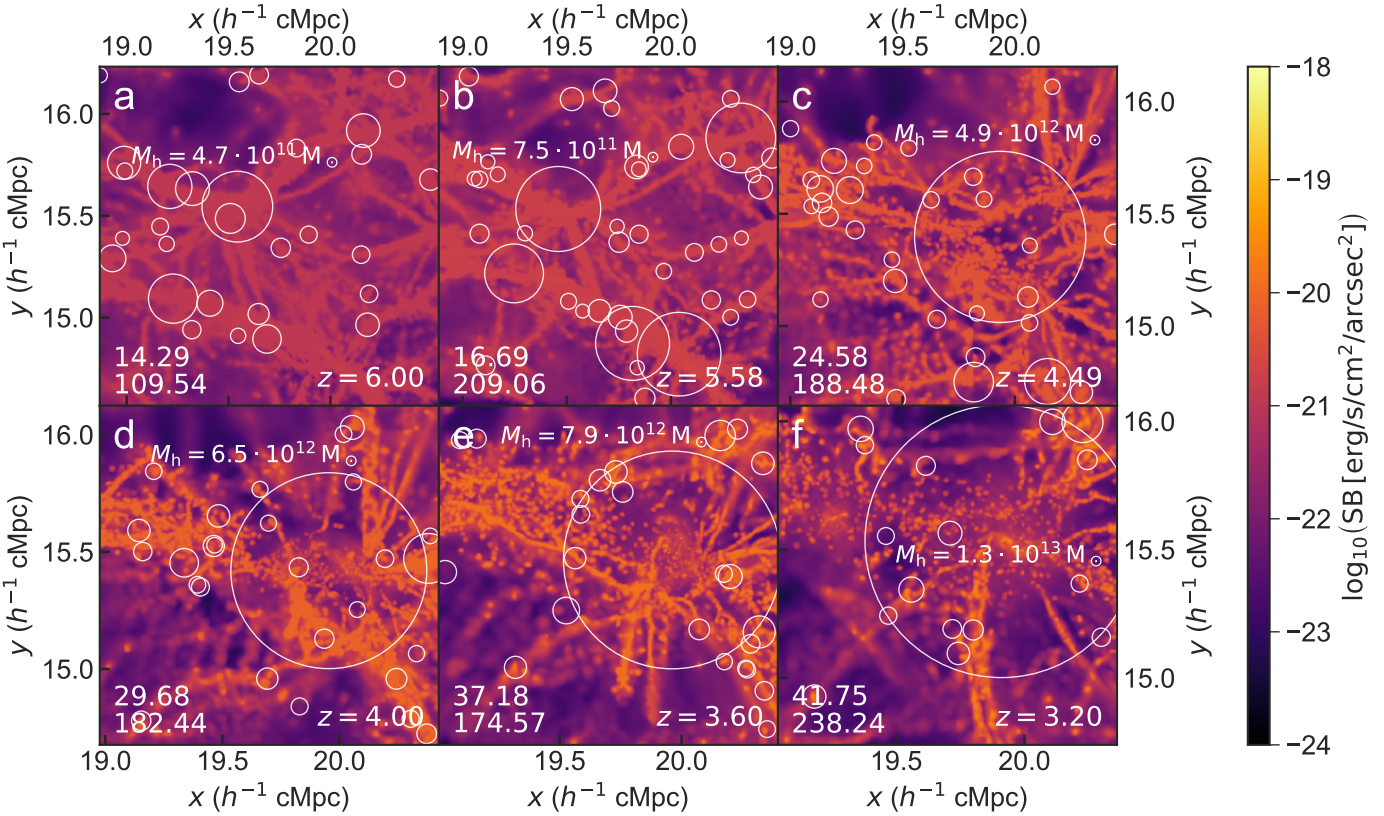

Fig. A.3. Lyα SB for a combination of recombination emission (of all gas in the simulation) below the mirror limit and collisional excitation of gas below half the critical self-shielding density at different redshifts. Both the mirror limit and the critical self-shielding density evolve as a function of redshift (see Fig. 1). The panels show snapshots at redshifts of $z = 6.00$, $z = 5.58$, $z = 4.49$, $z = 4.00$, $z = 3.60$, $z = 3.20$ for a narrowband with $\Delta\lambda_{\mathrm{obs}} = 3.75$ Å; at $z = 5.76$; this corresponds to $\sim 1.19\,h^{-1}$ cMpc, but this again changes with redshift. The panels all display a pixel grid of 300×300 and the angular size of the MUSE FOV (1×1 arcmin^2), which translates to different physical sizes at each corresponding redshift. The regions are all centred at the same comoving transverse coordinates as panel d in Figs. 8 and 10; however, the narrowband centre (the coordinate along the line of sight) has been chosen to coincide with the most massive halo in each panel to ensure the entire filament is captured in each panel. The two numbers in the bottom left corner show the same two different measures of the overdensity of the region, Δ_{baryon} and Δ_{halo} (see Sect. 3.4.1 for more details). Halos with halo mass of $M_{\mathrm{h}} > 10^{9.5}\,M_\odot$ are shown as circles, their size indicating their projected virial radius. The most massive halo in each panel is annotated. The scale varies between different panels since the angular size is kept constant across all redshifts.

Appendix B: Lyα optical depth

This work does not contain treatment of Lyα line radiative transfer effects (Sect. 2.4.2). For our purposes, the treatment without radiative transfer gives us valuable insights into the lower-density IGM filaments on large, cosmological scales without having to resort to implementing computationally expensive radiative transfer methods that are difficult to accurately model, for example because the effects of dust are poorly constrained.

In Fig. A.1, a two-dimensional density histogram for each of 2048 pixels in mock Lyα absorption spectra along 5000 lines of sight at $z = 4.8$ is shown as a function of both the Lyα optical depth τ and overdensity $\rho/\bar{\rho}$ in the relevant pixel. These spectra are extracted on the fly at redshift intervals $\Delta z = 0.1$ and are constructed from the gas density and neutral fraction, temperature, and peculiar velocity of neutral hydrogen along these lines of sight (for details, see Bolton et al. 2017, where they are studied in the context of the Lyα forest). The peculiar velocity of the gas in a given pixel has been used to translate its position to redshift space where optical depth is determined. Therefore both density and optical depth are effectively measured at line centre. The optical depth was divided by a factor of 2 to account for the fact that on average only half of the matter is in between the source and the observer; the other half is located behind the source[5]. From this figure, it is clear that at mean density optical depths of order 10 are reached, indicating that radiative transfer has an effect on most regions. However, effectively this plot still shows an overestimated measure of optical depth. Since it uses a measure of optical depth at line centre, this does not mean that physically no Lyα emission is detected in the optically thick regime ($\tau > 1$). Many Lyα photons may be able to escape because an initial scattering not only changes the direction of propagation of photons, but also shifts their frequency and the optical depth decreases quickly when moving away from line centre. An example of this effect is the Lyα radiation from galaxies, where densities are high enough to have optical depths of the order of 10^6, but escape away from line centre is still possible. The optical depth thus mostly informs the expected degree of scattering, that is spatial and spectral broadening of the line profile.

Additionally, the neutral hydrogen (H I) column density at $z = 4.8$ is shown in Fig. A.2 for precisely the same simulation region (and density limits used for collisional excitation) as in Fig. 8, with the same narrowband width of $\Delta\lambda_{\rm obs} = 3.75$ Å (equivalent to $\sim 1.19\,h^{-1}$ cMpc), and pixel grids of pixel grid of 1024×1024 (panel a) and 300×300 (panels b–d). The overview map (panel a) shows that all areas have column densities of at least $N_{\rm HI} \sim 10^{15}\,{\rm cm}^{-2}$. The most extreme features of the low-density gas show column densities of 10^{17}–$10^{18}\,{\rm cm}^{-2}$, which is the range of Lyman-limit systems. Except for the self-shielding prescription, simulations that are very similar to that used in this work are found to match observational H I column density distributions well at lower redshifts, where data are more abundant, at least up to $N_{\rm HI} \sim 3 \cdot 10^{16}\,{\rm cm}^{-2}$, where self-shielding is expected to have a negligible effect (Bolton et al. 2017). At higher column densities, the self-shielding prescription that we use (Rahmati et al. 2013) was calibrated to yield realistic column density distributions. At the highest column densities, our simulation will certainly be affected by our simplistic galaxy formation model. These high densities are, however, not the focus of this study.

As with Fig. A.1, it has to be taken into account that this is the column density projected for the entire narrowband. Emitting structures seen within this slice always lie between the boundaries of this region. Therefore part of the column density that is projected may be behind the emitting region, as seen from the observer's perspective. This means that, on average, the actual values of column densities photons travels through is about half of what is displayed.

As discussed in Sect. 2.4.2, it is expected that the precise way in which these scattering processes affect the perceived SB images are the result of a competition between two underlying effects. One possibility is that the photons emerging from the filamentary structure might be spread out, causing the signal to become fainter. The second possibility is that the filament signal might be enhanced by Lyα radiation coming from nearby dense structures (where additional radiation is likely to be produced in galaxies) that is scattered in the filament, thereby causing the filaments to appear brighter. As mentioned, similar simulations including radiative transfer show a mixture of these two effects, where the SB of filaments generally is not affected much or even boosted (private communication, Weinberger, 2019).

Appendix C: Redshift evolution

The region extensively discussed in Sect. 3.4, shown in panel d of Fig. 8 and all panels in Fig. 10, is shown at different redshifts in Fig. A.3, again showing the combination of recombination emission of all gas in the simulation below the mirror limit and collisional excitation of gas below half the critical self-shielding density. The panels shown are centred at the same transverse comoving coordinates as panel d in Fig. 8 and all panels in Fig. 10, but the narrowband centre (the coordinate along the line of sight) is now chosen to coincide with the most massive halo in each panel to ensure the same structure is captured in each panel. Each panel covers the angular size of the MUSE FOV, the physical extent of which varies at different redshifts.

Following the redshift evolution from high to low (going from panel a to panel f), we note that the comoving size of the observed region shrinks roughly from $\sim 1.5 \times 1.5\,h^{-2}\,{\rm cMpc}^2$ to just over $\sim 1 \times 1\,h^{-2}\,{\rm cMpc}^2$ since the angular size of the FOV is kept fixed at $1 \times 1\,{\rm arcmin}^2$. The appearance of new massive ($M_{\rm h} > 10^{9.5}\,M_\odot$) halos and their evolution in relative movement and mass accretion, indicated by the increase in their virial radii, can also be traced between the different panels. Panel e, at $z = 3.60$, has the same redshift as shown in the bottom two panels of Fig. 10.

With these conservative limits that exclude emission from the dense (and complicated) central regions of halos, Lyα emission appears brighter at low redshift, where the mirror limit is less affected by SB dimming and self-shielding effects only start to play a role at higher overdensities, as discussed in Sect. 3.4.2. Panels a and b appear particularly homogeneous as large portions are impacted by the mirror limit (24.6% and 22.1% of pixels exceeding the mirror limit). We note that at low redshift, on the other hand, there is less low-density gas that is luminous in Lyα, especially within the large, central halo. The gas there is likely denser and hotter and thus less effective at emitting Lyα radiation, at least within the low-density regime that we are considering (cf. Figs. 3 and 6 and their discussion in the text).

[5] We note that the division by 2 is necessary as the Lyα optical depths were originally extracted to study Lyα forest absorption in the spectra of background sources in which case all the gas that affects a pixel in redshift space is in front of the source in real space.